Applied Catalysis B: Environmental 317 (2022) 121703

Contents lists available at ScienceDirect

Applied Catalysis B: Environmental

journal homepage: www.elsevier.com/locate/apcatb

Electrodeposition of nanostructured Bi_2MoO_6@Bi_2MoO_{6-x} homojunction films for the enhanced visible-light-driven photocatalytic degradation of antibiotics

Elvira Gómez [a,b,*], Roberto Cestaro [c], Laetitia Philippe [c], Albert Serrà [a,b,*]

[a] Grup d'Electrodeposició de Capes Primes i Nanoestructures (GE-CPN), Departament de Ciència de Materials i Química Física, Universitat de Barcelona, Martí i Franquès, 1, E-08028 Barcelona, Catalonia, Spain
[b] Institute of Nanoscience and Nanotechnology (IN2UB), Universitat de Barcelona, Barcelona, Catalonia, Spain
[c] Empa, Swiss Federal Laboratories for Materials Science and Technology, Laboratory for Mechanics of Materials and Nanostructures, Feuerwerkerstrasse 39, CH-3602 Thun, Switzerland

ARTICLE INFO

Keywords:
Photocatalysis
Antibiotics
Aurivillius
Water decontamination
Homojunction
LEDs

ABSTRACT

Complex tunable visible-light-driven Aurivillius-phase-based micro- and nanostructured photocatalysts were fabricated following a novel, scalable, easily implemented sequential process based on electrochemical deposition and thermal treatment. Regarding its novelty, electrochemistry was the primary tool for synthesis, one that constitutes a viable alternative to other complex chemical and physical processes. The parameters of electrodeposition and thermal conditions promoted different nanostructured Bi_2MoO_6 and Bi_2MoO_6@Bi_2MoO_{6-x} films. The nanostructured homojunction Bi_2MoO_6@Bi_2MoO_{6-x} films obtained after 3 h of calcination showing micro- and nanowire morphology emerged as the most effective photocatalyst for degrading and mineralizing the mono- and multiantibiotic solutions (i.e., tetracycline, ciprofloxacin, and/or levofloxacin), which achieved near-total degradation and exceptionally high mineralization values (>95%) after 180 min of radiation. The materials' proven reusability, low photocorrosion activity, and excellent photocatalytic performance in mineralizing antibiotics can support the implementation of Bi_2MoO_6@Bi_2MoO_{6-x} homojunctions as efficient visible-light photocatalysts under solar radiation.

1. Introduction

The inevitable increase in the consumption of antibiotics derived from livestock industries and medicine has continued to alter microbial communities and promoted the emergence of antibiotic-resistant strains [1–3]. Growing concern over the risk posed by antibiotic-resistant microorganisms to human health, with an annual death toll estimated to rise to 10 million by 2050, have prompted global actions to counter antimicrobial resistance [4–6]. Among them, the strategies and technologies applicable the world over, including in developing countries, for removing antibiotic pollution from the environment, especially in bodies of water, and consequently reducing the occurrence of antibiotic-resistant microorganisms have been pivotal but continue to require further development [7,8].

Heterogeneous photocatalysis has recently attracted attention among researchers for treating different wastewaters. The photocatalytic treatment of wastewater is based on the generation of highly reactive oxidizing species, including hydroxyl radicals, that can mineralize organic matter into carbon dioxide and inorganic salts when the semiconductor's surface absorbs photons with energy equal to or greater than the semiconductor's band gap [9,10]. Semiconductors with large band gaps (e.g., ZnO and TiO_2), which require UV-light energy and are thus inefficient under sunlight irradiation (i.e., ~5% UV, ~43% visible, and ~52% infrared), have traditionally been studied [11–13]. Although using sunlight to meet both economic and environmental criteria makes heterogeneous photocatalysis especially attractive, its potential application requires the development of chemically and photochemically stable photocatalysts that are efficient, especially under visible-light irradiation [11,14,15].

Aurivillius-related oxide family ($Bi_2A_{n-1}B_nO_{3n+3}$), consisting on an

* Corresponding authors at: Grup d'Electrodeposició de Capes Primes i Nanoestructures (GE-CPN), Departament de Ciència de Materials i Química Física, Universitat de Barcelona, Martí i Franquès, 1, E-08028 Barcelona, Catalonia, Spain.
E-mail addresses: e.gomez@ub.edu (E. Gómez), a.serra@ub.edu (A. Serrà).

https://doi.org/10.1016/j.apcatb.2022.121703
Received 24 March 2022; Received in revised form 30 June 2022; Accepted 2 July 2022
Available online 6 July 2022

intergrowth of $(Bi_2O_2)^{2+}$ sheets and perovskite blocks $(A_{n-1}B_nO_{3n+1})^{2-}$ that contain a layer of octahedral B sites, are potential visible-light-driven photocatalysts for water decontamination [16–18]. In particular, Bi_2MoO_6, with a small band gap of 2.5–2.8 eV, exhibits improved visible-light photocatalytic activity for mineralizing organic pollutants despite the rapid recombination of photoinduced charge carriers [19,20]. In past work, thermal treatments as well as the formation of Bi_2MoO_6-based homo- and heterojunctions have significantly improved the quantum yield by reducing the recombination process [21–23].

To date, Bi_2MoO_6-based materials have been prepared using various physical and chemical techniques, including coprecipitation, solvothermal deposition, hydrothermal deposition, and chemical vapor deposition [20,24–26]. However, electrodeposition has rarely been employed, despite its simplicity, excellent control of reaction parameters, and modest requirements in terms of technology and cost. To the best of our knowledge, few studies have demonstrated the feasibility of using electrochemical deposition to synthesize Bi_2MoO_6, and none have involved analyzing or optimizing the electrodeposition process [27–31]. Regardless of the route of synthesis, Bi_2MoO_6 is not directly deposited, and thermal treatment is usually required to promote the perpetual formation of different Aurivillius phases. However, the duration and temperature of thermal treatment are critical factors in forming Bi_2MoO_6, for some Bi oxides can sublimate. Thermal treatment is not only a critical stage in the production of Bi_2MoO_6 but also allows the formation of homo- and heterojunction architectures as well as increases the surface's oxygen vacancies. By extension, both effects heavily influence the separation and migration of photogenerated electrons and holes, thereby reducing the recombination losses and consequently enhancing the photocatalytic performance compared with bare Bi_2MoO_6 photocatalysts [21,23]. The formation of Bi_2MoO_6/Bi_2MoO_{6-x} homojunctions and the density of the surface's oxygen vacancies depend significantly on the annealing temperature and duration of the treatment [21–23]. Relatively low temperatures (i.e., low atomic diffusion rate across the surface into the bulk) facilitate the formation of an equidistribution of oxygen vacancies throughout the Bi_2MoO_6 structure, whereas higher temperatures (i.e., high atomic diffusion rate across the surface into the bulk) may enable the formation of an oxygen-deficient stoichiometric shell, which consequently results in the formation of a Bi_2MoO_6/Bi_2MoO_{6-x} homojunction. In the process, the formation of the homostructure of Bi_2MoO_6/Bi_2MoO_{6-x} strongly depends on the duration of the annealing treatment [21–23].

In our systematic study, the sequential synthesis of Bi_2MoO_6/Bi_2MoO_{6-x} homojunction nanostructured films was performed using a simple electrodeposition process followed by thermal treatment. The synthesized Bi_2MoO_6/Bi_2MoO_{6-x} homojunction films were characterized according to various analytical techniques, and their photocatalytic performance was evaluated by the photocatalytic mineralization of single-pollutant solutions (20 ppm, 100 mL, pH = 7) of the antibiotics tetracycline (TET), ciprofloxacin (CIP), and levofloxacin (LEV) and multipollutant antibiotic solutions (60 ppm, 100 mL, pH = 7) of TET (20 ppm), CIP (20 ppm), and LEV (20 ppm) under LED visible-light irradiation. Last, their photochemical stability was investigated during 120 h of continuous LED visible-light irradiation to determine the amount of Mo and Bi ions in solution. Among the results, the Bi_2MoO_6/Bi_2MoO_{6-x} nanostructured films exhibited 7–9 times more photocatalytic activity than pure Bi_2MoO_6, depending on the pollutant, as well as excellent reusability for all of the antibiotics and negligible photocorrosion. In this paper, the possible photocatalytic mineralization mechanism of the Bi_2MoO_6/Bi_2MoO_{6-x} nanostructured films is discussed as well. The findings and their implications may advance the electrochemical synthesis of Aurivillius-related oxide photocatalysts for water treatment and inspire the development of improved photocatalysts.

2. Experimental

2.1. Electrodeposition of nanostructured Bi_2MoO_6 films

Bismuth nitrate ($Bi(NO_3)_3{\cdot}5H_2O$, Sigma- Aldrich, ≥98%), sodium molybdate ($Na_2MoO_4{\cdot}2H_2O$, Fluka, ≥99.0%), and disodium ethylenediaminetetraacetate ($Na_2EDTA{\cdot}2H_2O$, Sigma-Aldrich, ≥99.0%) were used to prepare the electrochemical bath. All the solutions were prepared using MilliQ treated water. The electrochemical bath containing 4 mM $Bi(NO_3)_3$ + 8.5 mM $Na_2MoO_4{\cdot}2\,H_2O$ + 5 mM Na_2EDTA was prepared by dissolving first $Bi(NO_3)_3.5\,H_2O$ and $Na_2EDTA{\cdot}2\,H_2O$ in water at a fixed temperature of 70 °C. After their dissolution, the molybdate precursor was added and dissolved. The pH of the solution was not adjusted and the temperature was maintained at 70 °C during the electrochemical study and electrodeposition of nanostructured Bi_2MoO_6 films. The solution was de-aerated by argon bubbling before each experiment and maintained under argon atmosphere during it.

The electrochemical experiments were performed in a three-electrode cell system connected to a microcomputer-controlled potentiostat/galvanostat (Autolab PGSTAT30) equipped with NOVA software. The working electrode was fluorine-doped tin oxide (FTO) substrate, with a geometrical area of 1 cm^2, which were cleaned with absolute ethanol, rinsed with MilliQ water, and dried with nitrogen gas. The counter electrode was a Pt spiral and the reference electrode was a $Ag|AgCl|Cl^-$ (3 M)$|NO_3^-$ (0.5 M) electrode. The nanostructured Bi_2MoO_6 films were potentiostatically electrodeposited under magnetic stirring (400 rpm) conditions. After the electrodeposition, the samples were cleaned exhaustively with MilliQ water, dried with nitrogen gas, and subjected to an annealing treatment for 1 and 3 h at 400 °C in air atmosphere. The annealing treatment was performed using a rapid thermal annealing equipment (Advanced Riko Mila 5050) with a heating ramp rate of 10 °C min^{-1}.

The nanostructured Bi_2MoO_6 films were characterized using different techniques. The surface morphology and architecture of electrodeposits were analyzed by using a field emission scanning electron microscopy (FE-SEM; Hitachi S-4800) equipped with an energy-dispersive X-ray spectroscopy (EDX) detector. The elemental composition was determined with an X-ray fluorescence (XRF; Fischerscope® X-RAY XDV®-SDD) equipment. The thickness of the films was measured using a Leica DCM 3D Confocal and Interferometer. The phase and crystallinity of films were established by X-ray diffraction (XRD; Bruker D8 Discovery diffractometer) in the Bragg–Brentano configuration with CuK_α radiation. The Brunauer–Emmett–Teller (BET) specific surface areas were determined using the N_2 adsorption-desorption isotherms at 77 K measured using a Micrometrics Tristar-II. The chemical states of nanostructured films were explored by X-ray photoelectron spectroscopy (XPS; PHI 5600 Multitechnique, Physical Electronics) measurements using a monochromatic X-ray source (Al K_α line = 1486.6 eV, 350 W). In situ electron paramagnetic resonance (EPR) measurements were performed using a Bruker 300E ESR spectrometer at 77 K. Raman spectra were acquired using a WITec Alpha 300 R confocal Raman microscope with a 532 nm laser. The optoelectronic properties were examined by collecting diffuse reflectance spectra using a Perkin Lambda 900 UV spectrophotometer, whereas the photoluminescence spectra were examined at room temperature by using a PerkinElmer LS-55 fluorescence spectrometer. The photocurrent and Mott–Schottky experiments were conducted in a three-electrode cell containing 0.5 M Na_2SO_4. Platinum wire and $Ag|AgCl|Cl^-$ (3 M)$|SO_4^{2-}$ (0.5 M) were used as counter and reference electrodes, respectively, on a CHI 660 C workstation. The prepared nanostructured Bi_2MoO_6 films were used as the working electrodes. The measurement process was performed using a potential range from –1.0 to +1.0 V (vs. Ag|AgCl) at a frequency of 200 kHz and an amplitude of 10 mV.

2.2. Degradation and mineralization of tetracycline

Single-pollutant solutions (20 ppm, 100 mL, pH= 7) of the antibiotics TET, CIP, and LEV and multipollutant antibiotic solutions (60 ppm, 100 mL, pH = 7) of TET (20 ppm), CIP (20 ppm), and LEV (20 ppm) were selected to test the photocatalytic activity of nanostructured Bi_2MoO_6 and Bi_2MoO_6/Bi_2MoO_{6-x} films under visible-light irradiation. Irradiation was provided by four 6.2 W LEDs (Irradiance = 90 mW cm^{-2}; Energy consumption= 7 kWh (1000 h)) with an UV cutoff filter ($\lambda > 400$ nm). The relative intensity in function of wavelength of each LED is depicted in Fig. S1. In a typical experiment, 4 pieces of 1×1 cm^2 of photocatalyst (approx. 30 mg) were added to 100 mL of single-pollutant or multipollutant solutions.

Prior to irradiation, the photocatalyst was kept in contact to the 20 mg L^{-1} TET, CIP and LEV solutions, respectively, for 1 h in dark conditions in order to ensure the establishment of the adsorption/desorption equilibrium. Photolytic experiments were performed in absence of photocatalyst also for a period of time of 150 min in the same irradiation conditions. A given time points during the adsorption and photolytic experiments, the TET, CIP and LEV content in the solution was measured by using UV–vis spectrophotometer (PerkinElmer Lambda 900 UV) through recording the characteristic absorbance at 357 nm for TET, 276 nm for CIP, and 286 nm for LEV.

For the photocatalytic degradation of single-antibiotic solutions, the solution containing the photocatalyst, was maintained under magnetic stirring (250 rpm) and at fixed temperature of 20.0 ± 0.1 °C in all the experiments. The temporal evolution of the concentration of TET, CIP and LEV solutions, respectively, during 150 min of irradiation in presence of Bi_2MoO_6 and Bi_2MoO_6/Bi_2MoO_{6-x} films was determined using a UV–vis spectrophotometer (UV-1800, Shimadzu Corporation) and LC-MS analyses. Importantly, based on the LC-MS analysis the main intermediates of TET, CIP and LEV were identified. The mineralization ratio was established by measuring the reduction in the total organic carbon (TOC) after 180 min under LED irradiation. The TOC content was measured using the high-temperature combustion method with a TOC-V_{CSH} equipment (Shimadzu) with a high-sensibility column. All experiments were performed in triplicate.

In order to prove the photostability and reusability of nanostructured Bi_2MoO_6 and Bi_2MoO_6/Bi_2MoO_{6-x} films, the photocatalysts were reused 15 times. After each cycle, the photocatalyst was subjected to an annealing treatment at 250 °C during 30 min to remove the surface organics. The surface morphology of nanostructured Bi_2MoO_6 films was examined by FE-SEM observation after the 15 reusability cycles. To further investigate the photostability of nanostructured Bi_2MoO_6 and Bi_2MoO_6/Bi_2MoO_{6-x} films the total concentration of bismuth ions in solution after 72 h of continuous LED irradiation was determined by using inductively coupled plasma-mass spectrometry (ICP-MS) measurements.

In order to identifying the active species involved in the photocatalytic degradation of TET, CIP and LEV, trapping experiments were performed via selective radical scavengers. Isopropyl alcohol (IPA; Sigma-Aldrich, >99.7%), benzoquinone (BQ; Sigma-Aldrich, >99.7%), or triethanolamine (TEOA; Sigma-Aldrich, >99%) were added until to attain a concentration of 1 mM to the reaction media for evaluating the effect of hydroxyl radicals, superoxide radicals, or photogenerated holes, respectively. The effect on the photocatalytic degradation of each quencher was determined by measuring the maximum absorption peak intensity of each pollutant using a UV–vis spectrophotometer (UV-1800, Shimadzu Corporation) after 150 min of irradiation. Additionally, the electronic spin resonance (EPR) spectra of DMPO-$^{\bullet}$OH and DMPO-$O_2^{\bullet-}$ were also investigated using a Bruker 300E ESR spectrometer.

3. Results and Discussion

3.1. Electrodeposition and characterization of nanostructured Bi_2MoO_6 and Bi_2MoO_6/Bi_2MoO_{6-x} films

To identify the most suitable deposition potential to electrodeposit Bi_2MoO_6 films, cyclic voltammetry was systematically used to monitor the electrochemical behavior of the bath (Fig. 1). Molybdate- and bismuth-free baths were also investigated in order to clarify the possible electrochemical process involved in the electrodeposition of Bi_2MoO_6 films. The ionic strength of the various electrochemical media was fixed and adjusted with KCl.

The voltammetric study of molybdate reduction under those conditions presented two clear reduction currents centered at − 0.4 V and − 0.9 V, represented respectively by R_1 and R_2 in Fig. 1a. Based on the

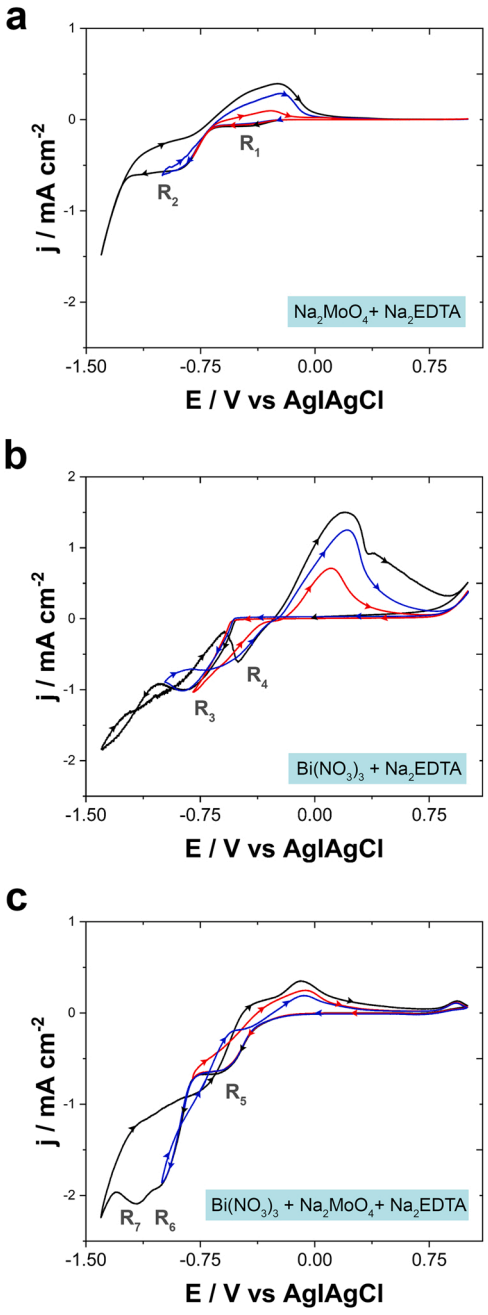

Fig. 1. : Cyclic voltammetry of (a) bismuth-free, (b) molybdate-free, and (c) bismuth–molybdate solutions on FTO substrate at 70 °C and 50 mV s^{-1}.

XRD and XPS analysis of the deposits prepared at − 0.4 V and − 0.9 V, the reduction currents were ascribed to the reduction of MoO_4^{2-} to Mo_xO_{3x-1}, predominantly Mo_4O_{11} (i.e., +6 to +5 oxidation state) and MoO_4^{2-} and/or Mo_xO_{3x-1} to MoO_2 (i.e., +6/+5 to +4 oxidation state), respectively. Depending on the pH of the electrochemical bath and the operating temperature, the two reduction currents could not be distinguished, thereby resulting in a broad reduction current band. When the operating temperature dropped below 55 °C, only a small signature of Mo_4O_{11} could be detected [32,33]. Although the transformation of MoO_4^{2-} to Mo_4O_{11} is more important when the operating temperature exceeds 55 °C, MoO_2 is the primary material obtained during the electrodeposition process. Among other results, a clear broad oxidation band centered at negative potentials was recorded in the anodic scan, and the oxidation current increased as the cathodic limit became progressively more negative (i.e., as hydrogen evolution becomes increasingly significant) but was minimized under a moderate flow of argon. Those dynamics can be attributed to the oxidation of hydrogen formed during the reduction process, because molybdenum oxides are excellent catalysts for the hydrogen evolution reaction [32–36].

By comparison, the voltammetric study of the molybdate-free bath revealed a clear reduction peak beginning at − 0.53 V (i.e., R_3 in Fig. 1b) that corresponded to the reduction of nitrate ions. The copious electrogeneration of hydroxide ions during nitrate electroreduction promoted the formation of $Bi(OH)_3$. However, at temperatures exceeding 55 °C, $Bi(OH)_3$ became dehydrated via a solid–solid phase transformation and thus caused the formation of Bi_2O_3, as confirmed by XRD and XPS analysis. Even so, the formation of Bi(0) was not detected by electrodeposition. Several studies have shown that dendrite-like Bi(0) deposits can be obtained from diluted nitric acid baths with $Bi(NO_3)_3$ + Na_2EDTA at room temperature [37,38]. Meanwhile, the reverse scan revealed the oxidation of the Bi(III) species.

Last, the voltammetric curves of molybdenum–bismuth bath also presented a clear reduction peak beginning at approximately − 0.3 V (i.e., R_5 in Fig. 1c) that corresponded to the codeposition of a mixture of bismuth oxides and molybdenum oxides. The EDS and XPS measurements of deposits prepared at − 0.6 V revealed the presence of bismuth,

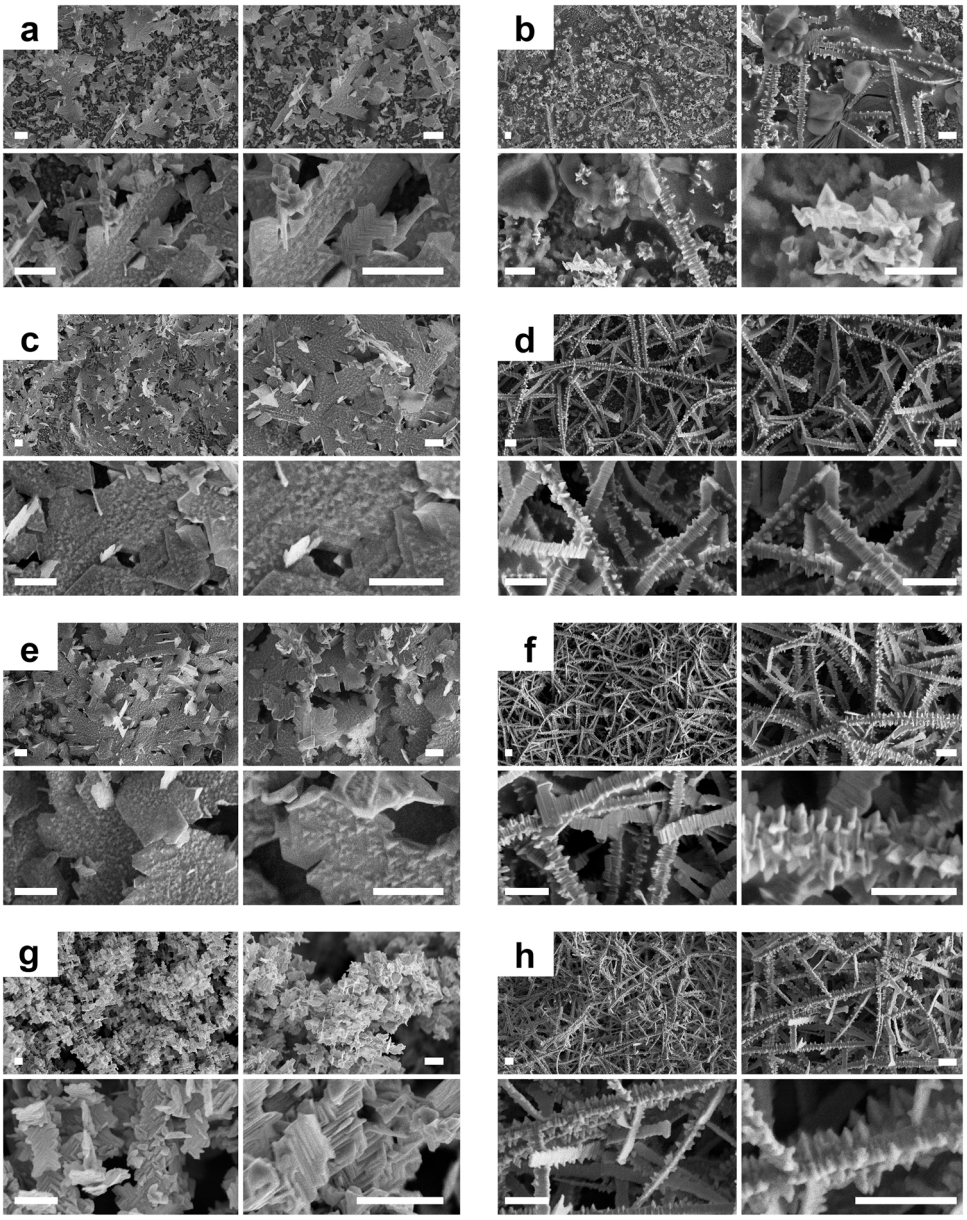

Fig. 2. : FE-SEM micrographs of electrodeposits prepared at (a, c, e, and g) − 0.9 V and (b, d, f, and h) − 1.3 V after circulating (a and b) 1 C cm^{-2}, (c and d) 2 C cm^{-2}, (e and f) 3 C cm^{-2}, and (g and h) 4 C cm^{-2}. Scale bar: 500 nm.

molybdenum, and oxygen. However, the amount of bismuth deposited was significantly less than that of molybdenum. The XRD pattern showed poor crystallization, and the weak peaks detected could not be clearly indexed to any phase of bismuth molybdates. The reduction currents observed in the voltammogram in Fig. 1c are hardly to attribute to a single process. For instance, although most bismuth was in the form of Bi(III), primarily as Bi_2O_3, the presence of Bi(0) was also detected by XPS at potentials more negative than − 1.2 V. That outcome was not observed in the molybdate-free bath, however (Fig. 1b). By contrast, in molybdenum's case, a mixture of Mo(V) and Mo(IV) oxides was observed regardless of the potential applied. Although those deposits were Mo-rich at potentials lesser than − 0.6 V, the relative amount of Mo increased from − 0.9 V to − 1.4 V. All deposits prepared at potentials between − 0.9 V and − 1.4 V exhibited low crystallinity, with weak peaks that could not be indexed with any phase of bismuth molybdate. Based on those data, potentials of − 0.9 V and − 1.3 V were selected to prepare the photocatalysts [27–29].

Fig. 2 depicts the morphology and architecture of the prepared films at − 0.9 V and − 1.3 V as a function of charge density. On the one hand, at − 0.9 V the deposits began to grow in the form of platelets or leaves, which facilitated the formation of a spongy architecture as the amount of deposited material increased. On the other, at − 1.3 V, despite a mixture of micro- and nanowires and small platelets at small charge densities similar to those obtained at − 0.9 V, the amount of deposited material dominated the presence of micro- and nanowires formed by nanocrystals as the circulated charge density increased. Both architectures had high specific surface areas. In the samples prepared at − 0.9 V and − 1.3 V and a charge density of 4 C cm^{-2} (Fig. 2g and h), BET specific surface area values of 33.5 and 46.8 m^2 g^{-1}, respectively, were obtained. Electrodeposits prepared at − 0.9 V had a greater relative amount of Bi than those prepared at − 1.3 V, and, regardless of the potential applied, the relative amount of Bi in the as-deposited films increased along with the charge density (Fig. 3a).

The XRD patterns of the as-electrodeposited films prepared at − 0.9 V and − 1.3 V under a charge density of 4 C cm^{-2} appear in Fig. 3b. All of the recorded peaks can be indexed well to cubic Bi_2O_3 (JCPDS: 16–0564) and orthorhombic Mo_4O_{11} (JCPDS: 65–2473) phases, and various peaks corresponded to SnO_2 from the FTO substrate. Because the molybdenum and bismuth oxides easily transformed into bismuth molybdates at temperatures exceeding 400 °C, a calcination process was required to obtain Bi_2MoO_6 and/or Bi_2MoO_6/Bi_2MoO_{6-x} films [21,39]. The annealing temperature and duration of the thermal treatment are key elements for obtaining Bi_2MoO_6 and for generating oxygen vacancies on the surface. They are also critical parameters that

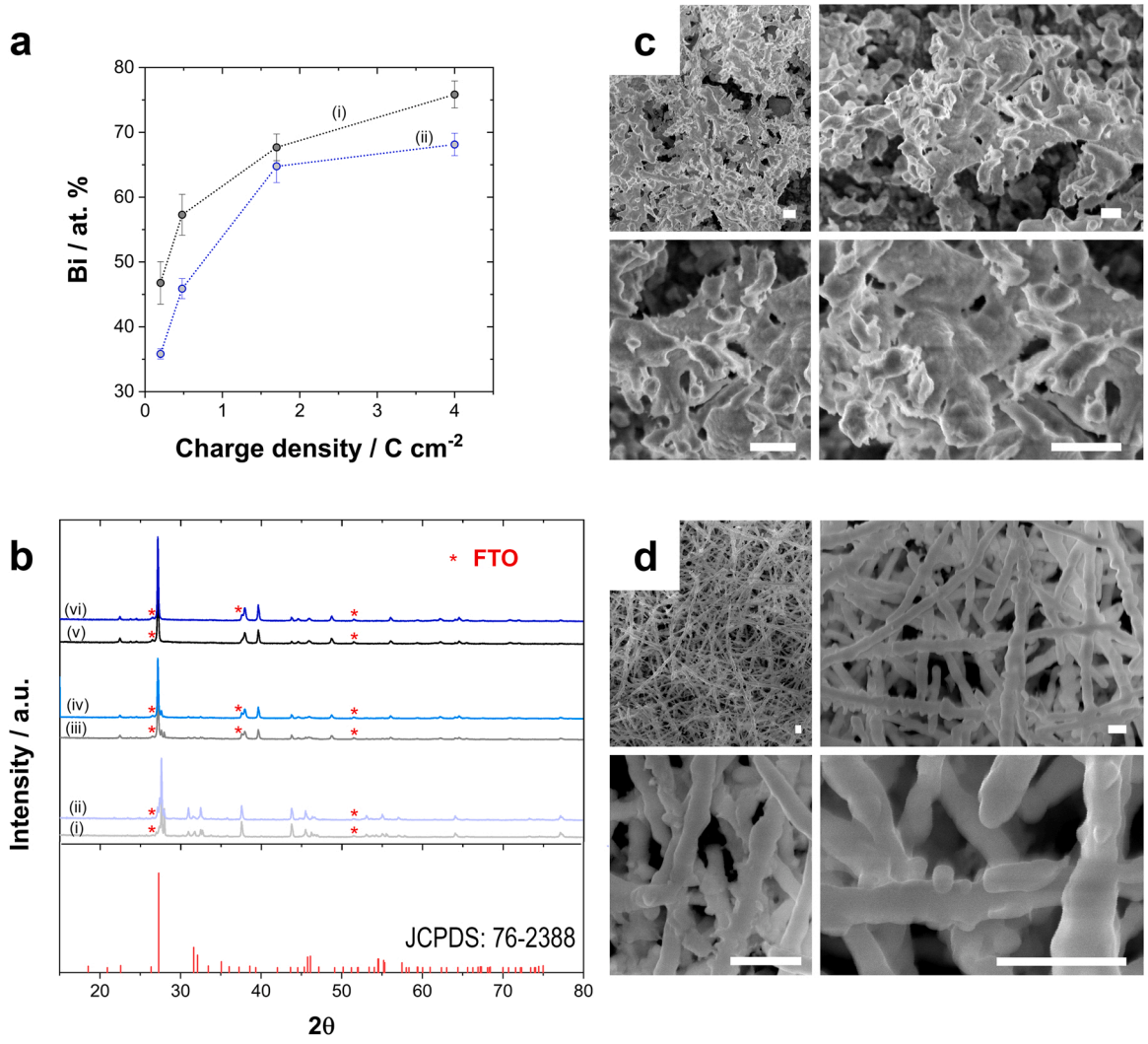

Fig. 3. : (a) Bismuth atomic percentage of electrodeposited films prepared at (i) − 0.9 V and (ii) − 1.3 V as a function of circulated charge density. (b) XRD pattern of electrodeposited films prepared at − 0.9 V (curves i, iii, and v) and − 1.3 V (curves ii, iv, and vi) after circulating 4 C cm^{-2} as prepared (curves i and ii) and after being annealed for 1 h (curves iii and iv) and 3 h at 400 °C in air atmosphere (curves v and vi). FE-SEM micrographs of electrodeposited films prepared at (c) − 0.9 V and (d) − 1.3 V after circulating 4 C cm^{-2} after being annealed for 3 h at 400 °C in air atmosphere, respectively. Scale bar: 500 nm.

affect the integrity of deposits, for some bismuth oxides, especially at the micro- and nanostructured level, can sublimate at temperatures exceeding 350 °C. In the study presented here, annealing temperature was optimized, 400 °C was selected, and the effect of the treatment time was analyzed [21]. The solid phase transformation of bismuth and molybdenum oxides into different phases of bismuth molybdates, the primary one being Bi_2MoO_6, and the atomic diffusion, specifically of oxygen, between the shell and core of the micro- and nanostructures allowed directly converting the Bi_2MoO_6 obtained into a novel core@-shell Bi_2MoO_6@Bi_2MoO_{6-x} homojunction. After annealing, the characteristic peaks of the orthorhombic Bi_2MoO_6 (JCPDS: 76–2388) could be detected, which confirmed the formation of Bi_2MoO_6. Comparing the diffraction patterns (Fig. 3b) of the samples after 1-h XRD patterns (iii) and (iv) and 3-h XRD patterns (v) and (vi) of thermal treatment revealed the same peaks. However, those peaks were slightly shifted to higher 2θ angles in the magnified XRD patterns due to the temperature-induced dislocation of oxygen atoms, which consequently induced a lattice contraction. That outcome was attributed to the formation of Bi_2MoO_{6-x} [21,40].

Regardless of the potential applied during electrodeposition, the same crystal structure was obtained in both cases. Fig. 3c and d illustrate the morphology and architecture of the deposits obtained after the 3 h of annealing treatment. The morphology of both films reduced after the annealing process and transformed into more rounded, finer shapes. As for the films prepared at − 0.9 V, a spongy morphology could be observed, whereas the films obtained at − 1.3 V demonstrated a network of micro- and nanowires with diameters between 120 and 300 nm. The BET specific surface area of both samples slightly exceeded those before the thermal treatment, with values of 36.4 and 49.8 $m^2\ g^{-1}$ at − 0.9 V and − 1.3 V, respectively (Fig. S2). Beyond that, some bismuth oxides could have been sublimated during annealing. Therefore, by modulating the applied potential during electrodeposition, the morphology and architecture of bismuth molybdate films could be easily modulated using the same solution, which implies another extra advantage of electrodeposition over other traditional synthetic processes.

To further analyze the surface chemistry of deposits annealed for 1 h and 3 h, the XPS spectra of Bi 4 f, Mo 3d, and O 1 s were investigated (Fig. 4). Once the data were calibrated with C as a reference (284.6 eV), the oxidation states of Bi and Mo were confirmed to be III and VI, respectively, in all samples, and the presence of Bi(II) and Mo(IV) was not detected. The high-resolution Bi 4 f XPS spectra of samples annealed for 1 h were deconvoluted in two peaks with respective binding energies of 159.33 and 164.58 eV and that were respectively assigned to the Bi^{3+} 4 $f_{7/2}$ and Bi^{3+} 4 $f_{5/2}$ signals [41]. However, after 3 h of annealing, the binding energy peaks shifted by approximately 0.18 eV for deposits prepared at − 0.9 V and by approximately 0.26 eV for deposits prepared at − 1.3 V compared with the samples annealed for 1 h due to the formation of oxygen vacancies on the photocatalyst's surface [42]. Those results are consistent with the formation of a core@shell Bi_2MoO_6@Bi_2MoO_{6-x} homojunction, being similar to results reported for Bi_2MoO_{6-x} in the literature [21,22]. The Mo 3d XPS spectra also exhibited two peaks centered at respective binding energies of 232.21 and 235.34 eV, which respectively correspond to Mo $3d_{5/2}$ and Mo $3d_{3/2}$. By contrast, in samples annealed for 3 h, the presence of oxygen vacancies distorted the Mo–O bond, and the binding energies shifted by approximately 0.15 eV for deposits prepared at − 0.9 V and by approximately 0.14 eV for deposits prepared at − 1.3 V compared with the samples annealed for 1 h [39]. The presence of defects in the surface oxygen increased the binding energy of Bi, thereby inducing electron transfer from the $(Bi_2O_2)^{2+}$ layer to the $(MoO_4)^{2-}$ layer and, in turn, enhancing the electron cloud density of Mo atoms [40]. As a result, the binding energy of Bi 4 f and Mo 3d were higher and lower, respectively, for core@shell Bi_2MoO_6@Bi_2MoO_{6-x} homojunction photocatalysts than for the Bi_2MoO_6 photocatalysts. In addition, in samples annealed for 3 h, an asymmetric O 1 s peak was observed, centered at binding energies greater than those of the broad O 1 s peak observed in samples annealed for 1 h. That outcome could be explained as a consequence of the high electron-attracting effect of adjacent oxygen vacancies. Moreover, the broad O 1 s peak of samples annealed for 1 h was deconvoluted into two peaks at respective binding energies of 529.8–529.9 and 530.9 eV corresponding to Bi–O and Mo–O coordination. The XPS analysis of samples annealed for 1 h revealed a negligible concentration of surface oxygen vacancies on the photocatalyst's surface. By contrast, the asymmetric O

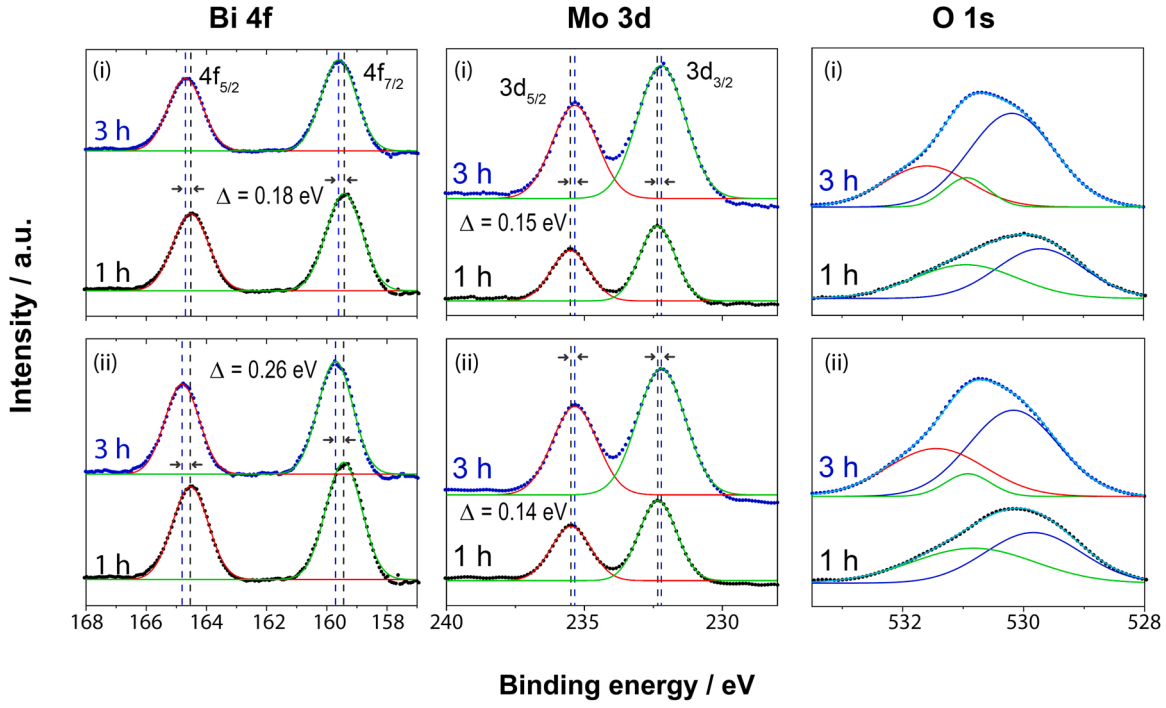

Fig. 4. : XPS spectra of Bi 4 f, Mo 3d, and O 1 s of electrodeposited films prepared at (i) − 0.9 V and (ii) − 1.3 V after circulating 4 C cm^{-2} and being annealed for 1 h and 3 h at 400 °C in air atmosphere.

1 s peak of samples annealed for 3 h was deconvoluted into three peaks at respective binding energies of 530.1, 530.9, and 531.7 eV corresponding to Bi–O, Mo–O, and oxygen vacancies.

Beyond that, the surface atomic concentration ratio of Bi 4 f to Mo 3d to O 1 s clearly confirmed the depletion of oxygen atoms after 3 h of annealing [21]. In sum, after 3 h of annealing treatment, surface oxygen vacancies were detected on the surface of the photocatalysts. All of those data are consistent with the formation of Bi_2MoO_6 and core@shell Bi_2MoO_6@Bi_2MoO_{6-x} homojunction photocatalysts after 1 h and 3 h of thermal treatment, respectively.

EPR is frequently used to investigate the presence of oxygen defects. In various materials such as TiO_2, ZnO, and, more recently Bi_2MoO_{6-x}, the *g* factor of approximately 2.001 has been attributed to oxygen vacancies [43–46]. Based on EPR measurements of deposits annealed for 1 h and 3 h, Fig. 5a shows that after 3 h of annealing, independently of the applied potential during deposition, a sharp, intense EPR signal was recorded, that corresponds to a g factor of approximately 2.003, which can be attributed to the electron-trapped center at the site of the oxygen vacancies [47,48]. However, the same result was also detected, albeit with a significantly lower intensity, after 1 h of annealing, which indicates that surface oxygen vacancies also formed after 1 h. Those results suggest that as the duration of annealing increases, the oxygen

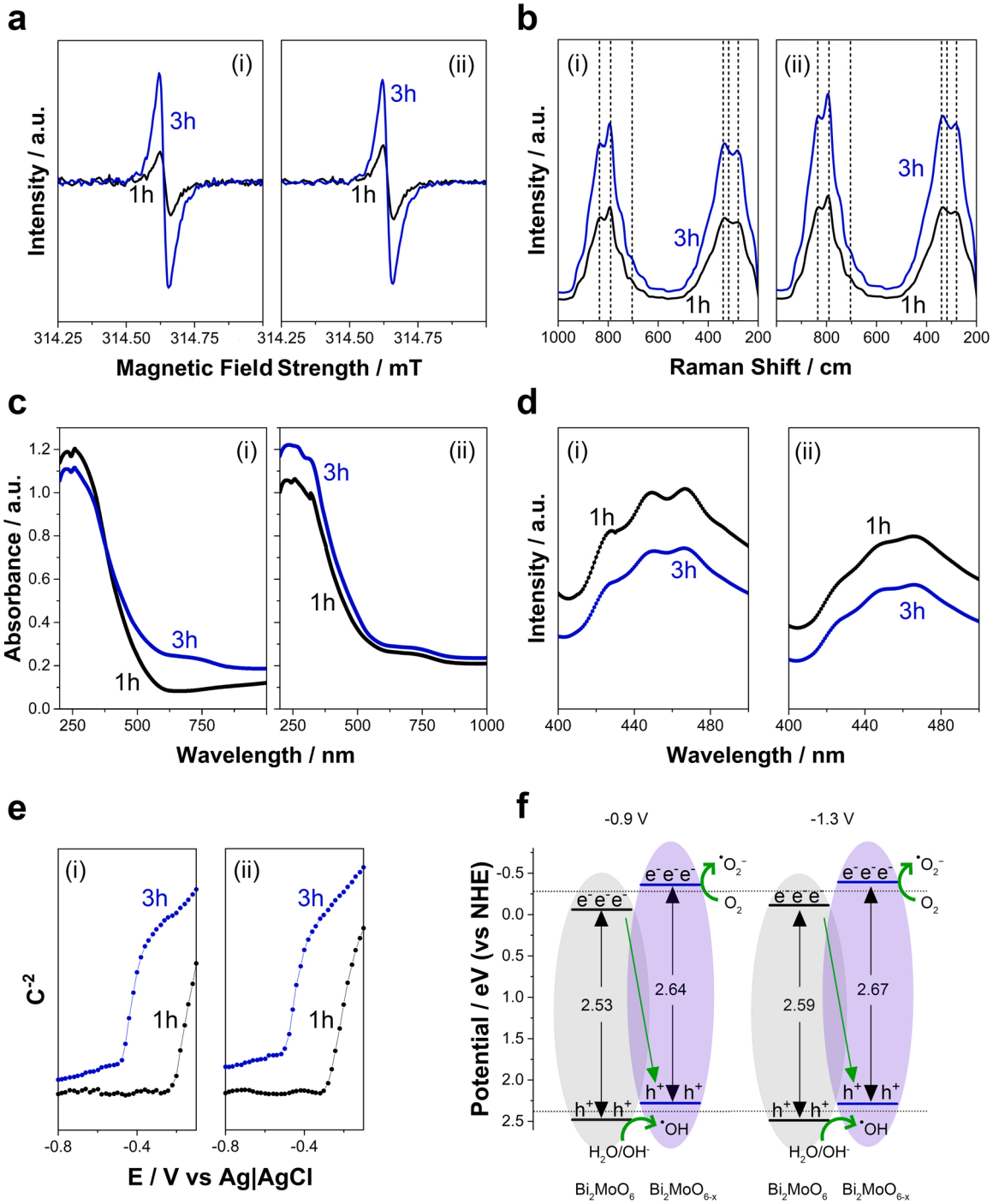

Fig. 5. : (a) EPR, (b) Raman, (c) UV–vis absorption, (d) PL spectra, and (e) Mott–Schottky plots of both electrodeposited films prepared at (i) − 0.9 V and (ii) − 1.3 V after circulating 4 C cm^{-2} and being annealed for 1 h and 3 h at 400 °C in air atmosphere. (f) Schematic representation of the photocatalytic mechanism of core@shell Bi_2MoO_6@Bi_2MoO_{6-x} homojunction photocatalysts prepared at − 0.9 V and − 1.3 V.

deficiency on the surface of the photocatalyst increases as well [47]. The results of Raman spectroscopy, shown in Fig. 5b, also indicate the formation of core@shell Bi_2MoO_6@Bi_2MoO_{6-x} homojunction photocatalysts after 3 h of annealing. Although the positions of the Raman peaks were nearly identical after 1 h and 3 h of annealing, the Raman intensity of all of the peaks was higher after 3 h of annealing. In addition, the relative peak intensity, especially for Raman peaks at 278, 321, and 348 cm^{-1} and assigned to Bi–O stretches and lattice modes, were higher after 3 h than 1 h of treatment, which demonstrates the contribution of oxygen vacancies to modify optoelectronic properties of photocatalysts. Meanwhile, the relative intensity of peaks located at 794, 709, and 839 cm^{-1}, which were assigned to A1g modes of an MoO_6 octahedron, indicate orthorhombic distortions of the octahedron both after 1 h and 3 h of annealing, which is also consistent with the formation of oxygen vacancies [46,49,50]. Therefore, XPS, EPR, and Raman spectral analyses confirmed the formation Bi_2MoO_6 during the annealing process as well as the formation of oxygen surface vacancies, which are more relevant after 3 h of annealing and lead to the formation of core@shell Bi_2MoO_6@Bi_2MoO_{6-x} homojunction photocatalysts.

The UV–vis DRS spectra of samples after 1 h and 3 h of annealing are depicted in Fig. 5c. The formation of surface oxygen vacancies, which appear after 1 h of annealing but are more prominent after 3 h of annealing, clearly affected the optoelectronic properties of Bi_2MoO_6 films. Bi_2MoO_6 exhibited a characteristic absorption sharp edge at 470 nm but was slightly redshifted in the prepared materials, especially after 3 h of annealing, due to the increased density of the surface oxygen vacancies. The formation of oxygen vacancies also enhanced absorbance in the range of 500–1000 nm, which was more marked in spongy films (i.e., prepared at −0.9 mV). The absorption of samples prepared at − 1.3 V, which have a network of micro- and nanowires architecture, was similar but slightly shifted after 1 h and 3 h of annealing. The architecture also affected the absorption of the photocatalysts, which reiterates earlier findings [9,13]. The bandgap energy of each photocatalyst was calculated with Tauc plots [3], and the calculated E_g values were 2.53 and 2.59 eV for Bi_2MoO_6 prepared at − 0.9 and − 1.3 V, respectively, and 2.64 and 2.67 eV for core@shell Bi_2MoO_6@Bi_2MoO_{6-x} prepared at − 0.9 and − 1.3 V, also respectively.

It is well known that thermally created defects such as oxygen vacancies can act as active centers for the adsorption of molecular oxygen [21,51]. In turn, molecular oxygen, as an electron scavenger, can react with photogenerated electrons and consequently reduce the recombination rate of photogenerated holes with electrons. That dynamic normally translates into the considerable enhancement of photocatalytic activity. Next, PL spectra were used to qualitatively investigate the recombination of the photogenerated electron–hole pairs of Bi_2MoO_6 and Bi_2MoO_6@Bi_2MoO_{6-x}. As shown in Fig. 5d, the PL intensity decreased after 3 h of annealing, which indicates that the homojunction hindered the recombination process, for weak PL intensity normally indicates a weak recombination rate of electron–hole pairs. Those results are consistent with the formation of Bi_2MoO_6 with a lower density of surface oxygen vacancies after 1 h of annealing and the formation of core@shell Bi_2MoO_6@Bi_2MoO_{6-x} homojunction photocatalysts after 3 h of annealing.

The Mott–Schottky analysis was performed to calculate the band edge positions of each photocatalyst. As shown in Fig. 5e, the positive slope of the Mott–Schottky plot suggested that the core@shell Bi_2MoO_6@Bi_2MoO_{6-x} homojunction photocatalysts are *n*-type semiconductors. The flat band position, as calculated from the *x* intercepts of the linear region, was –0.265 (deposition potential: −0.9 V, with 1 h of annealing), –0.316 (deposition potential: −1.3 V, with 1 h of annealing), –0.567 (deposition potential: −0.9 V, with 3 h of annealing), and − 0.598 V (deposition potential: −1.3 V, with 3 h of annealing) versus Ag|AgCl, with equivalent values of –0.060, –0.111, –0.362 and −0.393 V vs. NHE, respectively. In general, the conduction band potential (E_{CB}) for *n*-type semiconductors is generally more negative, at approximately − 0.1 or − 0.2 V, than its flat band potential. Even so, the flat band potential for *n*-type semiconductors is frequently considered to be the conduction band potential as well. Likewise, in the work presented here, the conduction band potential was approximated to be the flat band potential. Beyond that, the valence band potential (E_{VB}) of Bi_2MoO_6 and Bi_2MoO_6@Bi_2MoO_{6-x} was also calculated using Eq. 1:

$$E_{VB} = E_{CB} + E_g \quad (1)$$

Fig. 5f shows a schematic illustration of the band positions of E_{CB} and E_{VB} for the core@shell Bi_2MoO_6@Bi_2MoO_{6-x} homojunction photocatalysts. Because the band position of E_{VB} was much greater than that of the standard redox potentials of E ($^{\bullet}OH/OH^-$) = +1.99 V versus NHE and/or E ($^{\bullet}OH/H_2O$) = +2.38 V versus NHE, the photogenerated hole (h^+) can be expected to oxidize hydroxyl groups and water into $^{\bullet}OH$ radicals. At the same time, the band position of E_{VB} was more negative than that of the redox potential of E ($O_2/^{\bullet}O_2^-$) = −0.28 V versus NHE, which may have reduced the dissolved oxygen and thus generated $^{\bullet}O_2^-$ radicals. It should be noted, however, that $^{\bullet}OH$ can also be photochemically generated from $^{\bullet}O_2^-$ radicals. Considering the results, it can be concluded that the core@shell Bi_2MoO_6@Bi_2MoO_{6-x} homojunction system is a typical Z-scheme photocatalytic system, one that can promote the separation of photogenerated charge carriers, maximize the formation of more active radicals, and thus facilitate superior photocatalytic degradation and stability.

Photocurrent measurements are often used to study the electron transport migration behavior and electrical conductivity of photocatalysts. As shown in Fig. 6, the electron transport migration under the visible-light irradiation of core@shell Bi_2MoO_6@Bi_2MoO_{6-x} homojunction photocatalysts was significantly higher, approximately 3.7 times higher, than with Bi_2MoO_6. All of the films showed a stable photocurrent throughout the measurement without any significant photocurrent decay. The formation of surface oxygen vacancies favored the electron transport migration, which also benefited the photocatalytic performance. Based on the UV–vis, Mott-Schottky experiments, and PL spectra and photocurrent transients of the prepared films, Bi_2MoO_6@Bi_2MoO_{6-x} homojunctions can be used as efficient visible-light photocatalysts.

3.2. *Visible–light-driven photocatalytic mineralization of antibiotics*

The photocatalytic activities of the Bi_2MoO_6 and core@shell Bi_2MoO_6@Bi_2MoO_{6-x} homojunction photocatalysts were evaluated by degrading and mineralizing 100 mL of single-pollutant solutions containing TET, CIP, and LEV (20 ppm of each compound, 100 mL, pH = 7) and 100 mL of multipollutant solutions of TET (20 ppm), CIP (20 ppm),

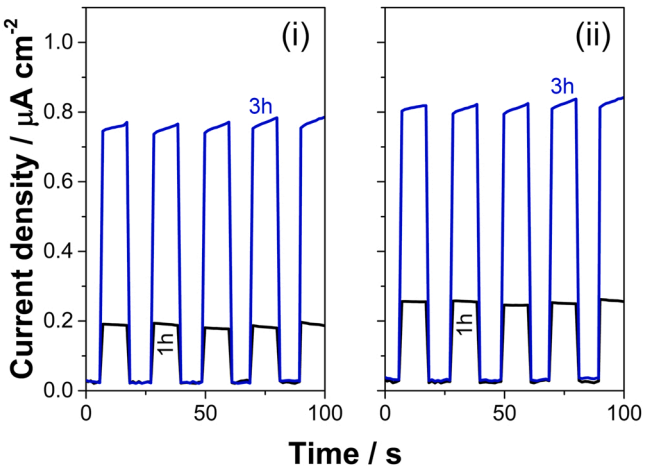

Fig. 6. : Transient photocurrent response of both electrodeposited films prepared at (i) − 0.9 V and (ii) − 1.3 V after circulating 4 C cm^{-2} and being annealed for 1 h and 3 h at 400 °C in air atmosphere.

and LEV (20 ppm), also at pH = 7, under artificial visible-light irradiation. The adsorption–desorption equilibria of single-pollutant solutions was examined before analyzing the photocatalytic performance of the Bi_2MoO_6 and core@shell Bi_2MoO_6@Bi_2MoO_{6-x} homojunction photocatalysts. With all materials, the three antibiotics reached a steady state in less than 60 min; however, adsorption varied depending on the antibiotic and the nature and effective area of the photocatalyst. The adsorption values when the adsorption–desorption equilibria were reached are summarized in Table 1.

As shown in Table 1, the antibiotic with the highest affinity for the surface of photocatalysts was TET, which can be attributed to the chemical nature of the photocatalyst's surface and the chemical structure of TET. In the case of TET, the core@shell Bi_2MoO_6@Bi_2MoO_{6-x} photocatalysts reached adsorption values approximately 2.3 times (E = –0.9 V, 3 h of annealing) and 2.9 times (E = –1.3 V, 3 h of annealing) larger than those of the Bi_2MoO_6 photocatalysts, while the effective specific surface areas were only 1.08 and 1.06 times larger in the Bi_2MoO_6@Bi_2MoO_{6-x} photocatalysts (E = –0.9 or −1.3 V, 3 h of annealing) than in their Bi_2MoO_6 counterparts (E = –0.9 or −1.3 V, 1 h of annealing). Therefore, the chemical nature of the photocatalyst's surface strongly determined its interaction with the different antibiotics, and the same trend was observed for CIP and LEV as well. At the same time, the increase in effective specific surface area when the chemical nature was similar clearly translated into an increase in adsorption capacity.

In parallel, the effect of light on the three antibiotics in the absence of a photocatalyst was also analyzed. Fig. S3 shows that photolytic degradation, over an irradiation period of 240 min, was negligible for all three antibiotics. In addition, the persistence of the pollutant in water was evaluated for 60 d under solar irradiation (i.e., natural light), and in all cases, the persistence of the contaminants was confirmed by reductions in the maximum absorbance less than 2%. Likewise, the TOC of all solutions was virtually constant.

After the adsorption–desorption equilibrium was reached, the irradiation of the photocatalyst with visible light began, which promoted the formation of reactive species capable of degrading the antibiotic. As illustrated in Fig. 7, the Bi_2MoO_6@Bi_2MoO_{6-x} photocatalysts had significantly higher photodegradation values regardless of the antibiotic; in fact, after only 60 min, degradations of more than 95% were reached in all cases. Note that the excellent photocatalytic performance for degrading antibiotics, despite being difficult to compare due to different experimental conditions, was equal to or even higher than state-of-the-art Bi_2MoO_6-based photocatalysts such as C_3N_4/Bi_2MoO_6/carbon and Bi_2MoO_6/Bi_2S_3 [52], surface oxygen vacancies modified Bi_2MoO_6 [53], $Bi_2Sn_2O_7$/Bi_2MoO_6, TaON/Bi_2MoO_6 core-shell [54], Ag-TiO_2/Bi_2MoO_6 [55], C_3N_4-Bi_2MoO_6-Bi [42], $CuInS_2$/ Bi_2MoO_6 [56], and $CuBi_2O_4$/Bi_2MoO_6 [57]. As for the Bi_2MoO_6 photocatalysts, after 150 min of visible-light irradiation, the degradation kinetics was significantly lower (see Table 2) and photodegradation values exceeded 95% for TET and CIP but were less than 90% for LEV for 71.9% and 86.2% of the films prepared at −0.9 V and −1.3 V, respectively. The ranking of the efficiency of the antibiotic photodegradation observed was as follows: Bi_2MoO_6 (–0.9 V) < Bi_2MoO_6 (–1.3 V) < Bi_2MoO_6@Bi_2MoO_{6-x} (–0.9 V) < Bi_2MoO_6@Bi_2MoO_{6-x} (–1.3 V). The photocatalysts prepared at −1.3 V exhibited superior photocatalytic performance to the ones prepared at −0.9 V favored also by their relatively higher effective specific surface areas.

Next, the kinetic analysis of the antibiotic degradations was performed based on the first-order kinetic model (see Figs. S4–S6). For example, in the case of TET, the annealing treatment enhanced the kinetic constant from 0.024 min^{-1} (–0.9 V, 1 h of annealing) to 0.055 min^{-1} (–0.9 V, 3 h of annealing) and from 0.031 min^{-1} (–1.3 V, 1 h of annealing) to 0.107 min^{-1} (–1.3 V, 3 h of annealing). The kinetic constant rose further with the increase of surface oxygen vacancies, which in turn favored electron transport migration and reduced the recombination processes. However, a comparison of the kinetic constants of the two Bi_2MoO_6@Bi_2MoO_{6-x} photocatalysts prepared at −0.9 V (0.055 min^{-1}) and −1.3 V (0.107 min^{-1}) revealed that the kinetic constant of the photocatalysts prepared at −1.3 V was approximately 2 times larger, while the effective specific surface area was approximately 1.37 times larger. Those differences align with the optoelectronic properties and photocurrent curves of photocatalysts, which suggests that the morphology and architecture of the samples prepared at −1.3 V, formed by a network of wires, probably facilitated the penetration of light. The same trend was observed for the degradation kinetics of CIP and LEV. However, comparing the degradation kinetics of the contaminants shows that in the case of the Bi_2MoO_6 photocatalysts, the antibiotic with the highest degradation kinetics was TET. The ranking of the degradation kinetics was thus as follows: TET > CIP > LEV. By contrast, in the case of the Bi_2MoO_6@Bi_2MoO_{6-x} photocatalysts, the antibiotic with the highest degradation kinetics was LEV, followed by TET and CIP. The chemical nature of the antibiotic and especially that of the photocatalyst's surface not only determined its interaction but also strongly affected its reactivity. Those differences can be explained as deriving from the type and amount of intermediate reactive species formed during the irradiation process in each case.

Following photodegradation, mineralization (i.e., total oxidation of the contaminant) was investigated as well. After 180 min of irradiation with visible light, TET achieved nearly total mineralization and both CIP and LEV more than 90% mineralization with the Bi_2MoO_6@Bi_2MoO_{6-x} photocatalysts. LEV's photodegradation was the quickest. In the case of the core@shell photocatalysts, mineralization was slightly less than that of TET; however, in terms of the type of catalyst, the trends were similar to those of photodegradation. The ranking of the efficiency of antibiotic mineralization was as follows: Bi_2MoO_6 (–0.9 V) < Bi_2MoO_6 (–1.3 V) < Bi_2MoO_6@Bi_2MoO_{6-x} (–0.9 V) < Bi_2MoO_6@Bi_2MoO_{6-x} (–1.3 V).

Based on the intermediates identified using LC-MS analysis, a mineralization mechanism can be proposed for each pollutant (see Figs. S7–S9). The proposed mechanisms are based on the MS spectra of aliquots of reaction media every 30 min of visible-light irradiation in the presence of a Bi_2MoO_6@Bi_2MoO_{6-x} (–1.3 V) photocatalyst. In TET's case (see Fig. S7), according to the charge-to-mass ratio (m/z), two possible pathways of the mechanism of mineralization were formulated, starting with the formation of the hydroxylated product $P_{TET}1$ or with the *N*-demethylation process giving rise to the product $P_{TET}2$. Successive attacks by holes and hydroxyl radicals promoted the fragmentation of intermediates via water loss, addition reactions, or the opening of rings and, in turn, induced the formation of the intermediates $P_{TET}3$, $P_{TET}4$, and $P_{TET}5$. Further oxidation resulted in the formation of the products $P_{TET}6$ and $P_{TET}7$, followed by carbon dioxide and other inorganic molecules [3,58]. In the case of CIP (see Fig. S8), two different possible pathways were formulated according the detected intermediates: (i) the gradual oxidative degradation of the lateral ring of piperazine, beginning with the ring-opening process, causing the formation of the product

Table 1
Adsorption capacity of TET, CIP, and LEV in relation to each photocatalyst in dark conditions after 60 min.

	Adsorption / %			
	Bi_2MoO_6 (−0.9 V)	Bi_2MoO_6@Bi_2MoO_{6-x} (−0.9 V)	Bi_2MoO_6 (−1.3 V)	Bi_2MoO_6@Bi_2MoO_{6-x} (−1.3 V)
TET (20 ppm)	6.2 ± 0.1	14.3 ± 0.2	9.1 ± 0.1	26.4 ± 0.2
CIP (20 ppm)	2.1 ± 0.2	4.3 ± 0.2	3.1 ± 0.2	7.8 ± 0.1
LEV (20 ppm)	4.5 ± 0.1	9.9 ± 0.1	5.9 ± 0.2	13.4 ± 0.1

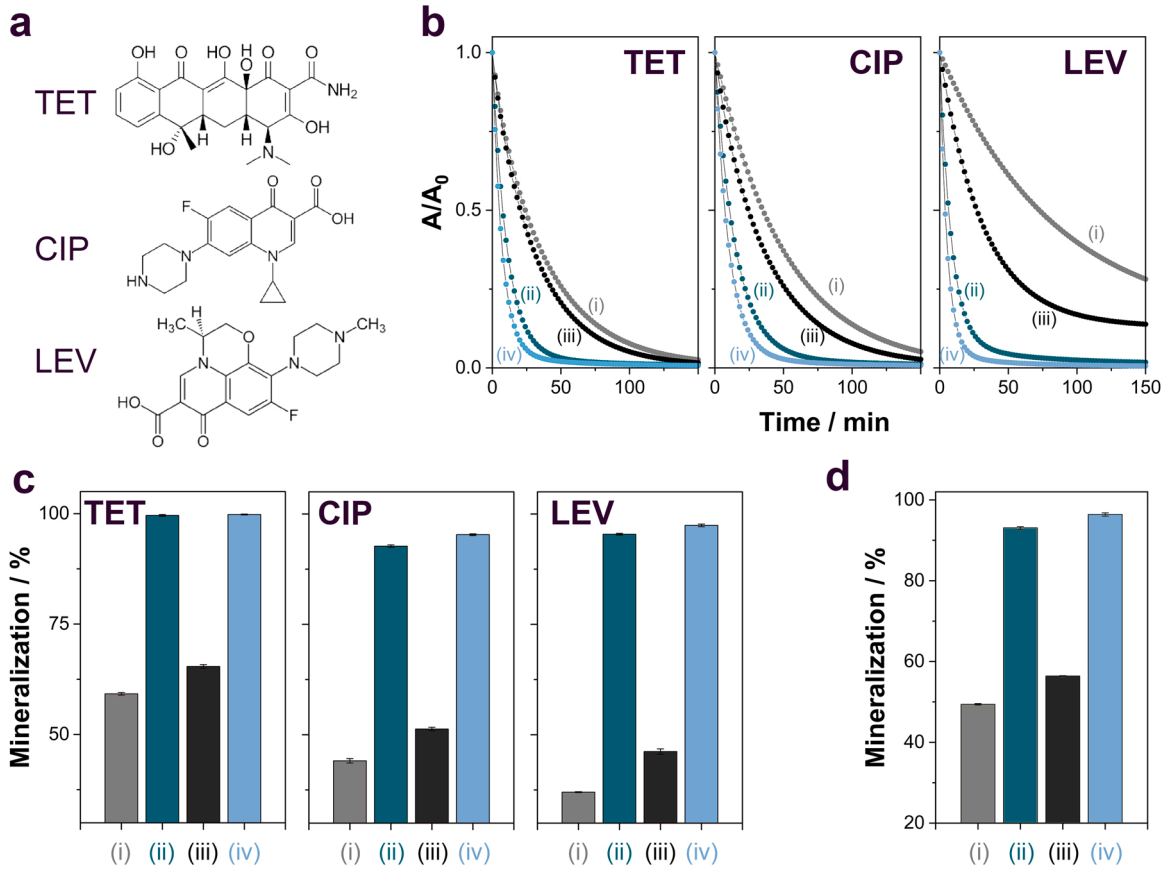

Fig. 7. : (a) Chemical structure of TET, CIP, and LEV. (b) Photodegradation and (c) mineralization of TET, CIP, and LEV (20 ppm of each compound, 100 mL, pH = 7) under 150 min of visible-light irradiation at 20 °C using electrodeposited films prepared at (i, ii) −0.9 V and (iii, iv) −1.3 V after circulating 4 C cm^{-2} and being annealed for (i, iii) 1 h and (ii and iv) 3 h at 400 °C in air atmosphere. (d) Mineralization of a multipollutant solution of TET (20 ppm), CIP (20 ppm), and LEV (20 ppm) at pH = 7 under 240 min of visible-light irradiation at 20 °C using electrodeposited films prepared at (i, ii) −0.9 V and (iii, iv) −1.3 V after circulating 4 C cm^{-2} and being annealed for (i, iii) 1 h and (ii and iv) 3 h at 400 °C in air atmosphere.

$P_{CIP}1$ and the subsequent loss of CO, $CH_2CH_2NH_2$, and COOH groups, and resulting in the formation of the intermediates $P_{CIP}2$, $P_{CIP}3$, and $P_{CIP}4$; and (ii) the substitution of fluorine by a hydroxyl group ($P_{CIP}5$) followed by decarboxylation ($P_{CIP}6$) and the opening of piperazine's lateral ring ($P_{CIP}7$). The above intermediates ultimately oxidized to carbon dioxide and other inorganic salts [59–62]. Last, the proposed degradation mechanism of LEV (Fig. S9) was based on three different pathways: (i) a process starting with the demethylation and hydroxylation reactions of LEV to form product $P_{LEV}1$, which subsequently is demethylated to product $P_{LEV}2$; (ii) a process starting with the decarboxylation of LEV evolving to product $P_{LEV}3$, which experiences either ring-opening and demethylation reactions to yield product $P_{LEV}4$ or the de-fluorination reaction of $P_{LEV}3$, thereby resulting in product $P_{LEV}5$; or (iii) the formation of product $P_{LEV}6$ as a result of the opening of the piperazinyl ring and demethylation and oxidation reactions. The above intermediates were further oxidized into smaller molecules and mineralized into carbon dioxide and simple inorganic species, and the mineralization process was confirmed by TOC analysis [54]. All of the proposed mechanisms are consistent with the literature [54,58,59,62,63].

The mineralization of a multipollutant solution of TET (20 ppm), CIP (20 ppm), and LEV (20 ppm), also at pH = 7, under 240 min of artificial visible-light irradiation using the Bi_2MoO_6 and Bi_2MoO_6@Bi_2MoO_{6-x} photocatalysts was investigated as well (see Fig. 7**d**). The mineralizing capacity of each photocatalyst was highly similar to that observed in the single-component solutions, again with the core@shell Bi_2MoO_6@Bi_2MoO_{6-x} homojunction photocatalysts being more efficient.

The reusability potential of the core@shell Bi_2MoO_6@Bi_2MoO_{6-x} homojunction photocatalysts was also studied in order to evaluate the applicability of the materials in real large-scale applications (see Fig. 8). To that purpose, reusability experiments were performed based on the reuse of photocatalysts within 15 successive photocatalytic runs. Although the efficiency of mineralization decreased slightly after 15 cycles, mineralization was consistently greater than 80% for the Bi_2MoO_6@Bi_2MoO_{6-x} photocatalysts (–0.9 V) and greater than 90% for the Bi_2MoO_6@Bi_2MoO_{6-x} photocatalysts (–1.3 V). Therefore, the decrease was less pronounced in deposits prepared at −1.3 V, which indicates the favorable reusability potential of the as-synthesized photocatalysts within successive runs of operation. After each cycle, the photocatalyst was subjected to 30 min of annealing treatment at 250 °C in order to remove adsorbed organics as well as regenerate the photocatalyst. Without that soft thermal treatment, the photocatalytic activity would have fallen approximately 10% faster. In addition, a morphological analysis of the surface of both catalysts showed no significant variations between them after 15 cycles (see Fig. 8b and d). Ultimately, after 15 reuse cycles, the phase and chemical nature of the photocatalysts showed no important variations (see Fig. S10).

Another factor that can strongly inhibit a photocatalyst's usability is photocorrosion and the consequent dissolution of the material, which results in the pernicious introduction of new inorganic pollutants into bodies of water. For all of the photocatalysts explored, the amount of bismuth and molybdenum was undetectable after 72 h of visible-light irradiation if an excess of antibiotic was added to the medium, which confirms that the dissolution of the photocatalysts resulted from a photoelectrochemical process involving charge carrier and not from a

Table 2
Photocatalytic degradation efficiency of 100 mL of single-pollutant solutions of TET, CIP, and LEV (20 ppm of each compound, 100 mL, pH = 7) and 100 mL of multipollutant solutions of TET (20 ppm), CIP (20 ppm), and LEV (20 ppm), at pH = 7, under artificial visible-light irradiation using the Bi_2MoO_6 and core@shell Bi_2MoO_6@Bi_2MoO_{6-x} homojunction photocatalysts.

	Bi_2MoO_6 (−0.9 V)			Bi_2MoO_6@Bi_2MoO_{6-x} (−0.9 V)			Bi_2MoO_6 (−1.3 V)			Bi_2MoO_6@Bi_2MoO_{6-x} (−1.3 V)		
	Degradation / %	k / min^{-1}	Mineralization / %	Degradation / %	k / min^{-1}	Mineralization / %	Degradation / %	k / min^{-1}	Mineralization / %	Degradation / %	k / min^{-1}	Mineralization / %
TET (20 ppm)	97.4 ± 0.5 (150 min)	0.024	59.2 ± 0.3	99.1 ± 0.6 (150 min)	0.074	99.6 ± 0.2	98.4 ± 0.3 (150 min)	0.031	65.5 ± 0.4	99.3 ± 0.5 (150 min)	0.107	99.8 ± 0.1
CIP (20 ppm)	94.9 ± 0.4 (150 min)	0.020	44.1 ± 0.5	98.8 ± 0.7 (150 min)	0.055	92.7 ± 0.3	97.3 ± 0.6 (150 min)	0.026	51.3 ± 0.4	99.2 ± 0.4 (150 min)	0.079	95.3 ± 0.2
LEV (20 ppm)	71.9 ± 0.6 (150 min)	0.010	37.0 ± 0.1	98.2 ± 0.4 (150 min)	0.087	95.4 ± 0.2	86.2 ± 0.5 (150 min)	0.023	46.2 ± 0.6	99.4 ± 0.6 (150 min)	0.119	97.4 ± 0.3
TET + CIP + LEV	–	–	49.4 ± 0.2	–	–	93.1 ± 0.3	–	–	56.4 ± 0.1	–	–	96.4 ± 0.4

purely chemical process. However, an examination of the amount of bismuth and molybdenum in pure water (i.e., in the absence of organic pollutants) after 72 h of visible-light irradiation showed that the photocatalysts prepared at −1.3 V exhibited less photocorrosion than those prepared at −0.9 V, especially in relation to bismuth, whose dissolved values ranged from 6% to 8% (–0.9 V) to undetectable amounts (–1.3 V). By contrast, molybdenum's dissolution was greater in the case of films prepared at −0.9 V for the Bi_2MoO_6 photocatalysts but practically identical in the case of the structure of the Bi_2MoO_6@Bi_2MoO_{6-x} photocatalysts regardless of the potential for preparation. That distinction demonstrated the potential of Bi_2MoO_6@$Bi_2MoO_{6-x}$to be used to eliminate contaminants. The same phenomenon was observed for other photocatalysts, in which organic contaminants acted as traps for charge carriers and other reactive species and consequently inhibited photocorrosive processes [3,64,65]. Ultimately, after the 72-h irradiation process, the specific surface areas of all of the photocatalysts were slightly reduced (see Fig. 8g). However, the non-detection of bismuth and molybdenum ions after 10 days of immersion in pure water in the dark or of any single- or multipollutant solutions, the maintenance of Bi_2MoO_6@Bi_2MoO_{6-x}'s photocatalytic performance in degrading and mineralizing antibiotics after those experiments, and the BET surface areas reinforce the proposal that the loss of stability of the Bi_2MoO_6@Bi_2MoO_{6-x} was a consequence of photocorrosion-related phenomena.

To investigate the role of reactive species of the core@shell Bi_2MoO_6@Bi_2MoO_{6-x} homojunction photocatalysts, trapping experiments were conducted by adding IPA, BQ, and TEOA as scavengers of $^{\bullet}OH$, $^{\bullet}O_2^-$, and h^+, respectively (see Fig. 9a and b). The TET degradation efficiency of core@shell Bi_2MoO_6@Bi_2MoO_{6-x} homojunction photocatalysts, of –99.1% and 99.3% for photocatalysts prepared at –0.9 and −1.3 V, respectively, decreased to approximately 29% (–0.9 V) or 26% (–1.3 V), 50% (–0.9 V) or 70% (–1.3 V), and 42% (–0.9 V) or 48% (–1.3 V) in the presence of hydroxyl radicals, superoxide radicals, and hole scavengers, respectively. The marked decrease after IPA was added demonstrates that the dominant factor during the degradation process was the hydroxyl radicals. Although $^{\bullet}OH$ was the predominant reactive species during photocatalytic degradation, the role of $^{\bullet}O_2^-$ and h^+ warrants consideration as well. Similar trends were observed for the other antibiotics analyzed. To further investigate the formation of reactive active species, EPR measurements were performed. After 5 min of visible-light irradiation, the signals of the DMPO–$^{\bullet}OH$ and DMPO–$^{\bullet}O_2^-$ adducts could be observed, which confirmed the formation of $^{\bullet}OH$ and $^{\bullet}O_2^-$ radicals during the reaction system. These findings are consistent with the previous results presented of the radical-scavenging experiments and confirm the important role of $^{\bullet}OH$ and $^{\bullet}O_2^-$ in degradation and mineralization.

4. Conclusions

Bi_2MoO_6 and core@shell Bi_2MoO_6@Bi_2MoO_{6-x} homojunction photocatalysts were synthesized via a simple process involving sequential electrodeposition and thermal treatment. The applied potential, the charge density, the annealing temperature, and the calcination time were found to influence the characteristics of the material. The optimized lower applied potential (–0.9 V) promoted platelet–sheet morphology, whereas micro- or nanowires were obtained at −1.3 V, the compositions of which exhibited different combinations between the oxides. After 1 h of calcination at 400 °C, a Bi_2MoO_6 structure was formed, while after 3 h, a novel complex core@shell Bi_2MoO_6@Bi_2MoO_{6-x} homojunction was obtained. The core@shell Bi_2MoO_6@Bi_2MoO_{6-x} homojunction photocatalysts exhibited excellent photocatalytic performance in degrading and mineralizing single- and multiantibiotic solutions (i.e., TET, CIP, and/or LEV), in which almost complete mineralization (>95%) was achieved after 180 min of radiation, especially using the deposit showing micro- or nanowire morphology. They also exhibited high reusability and low

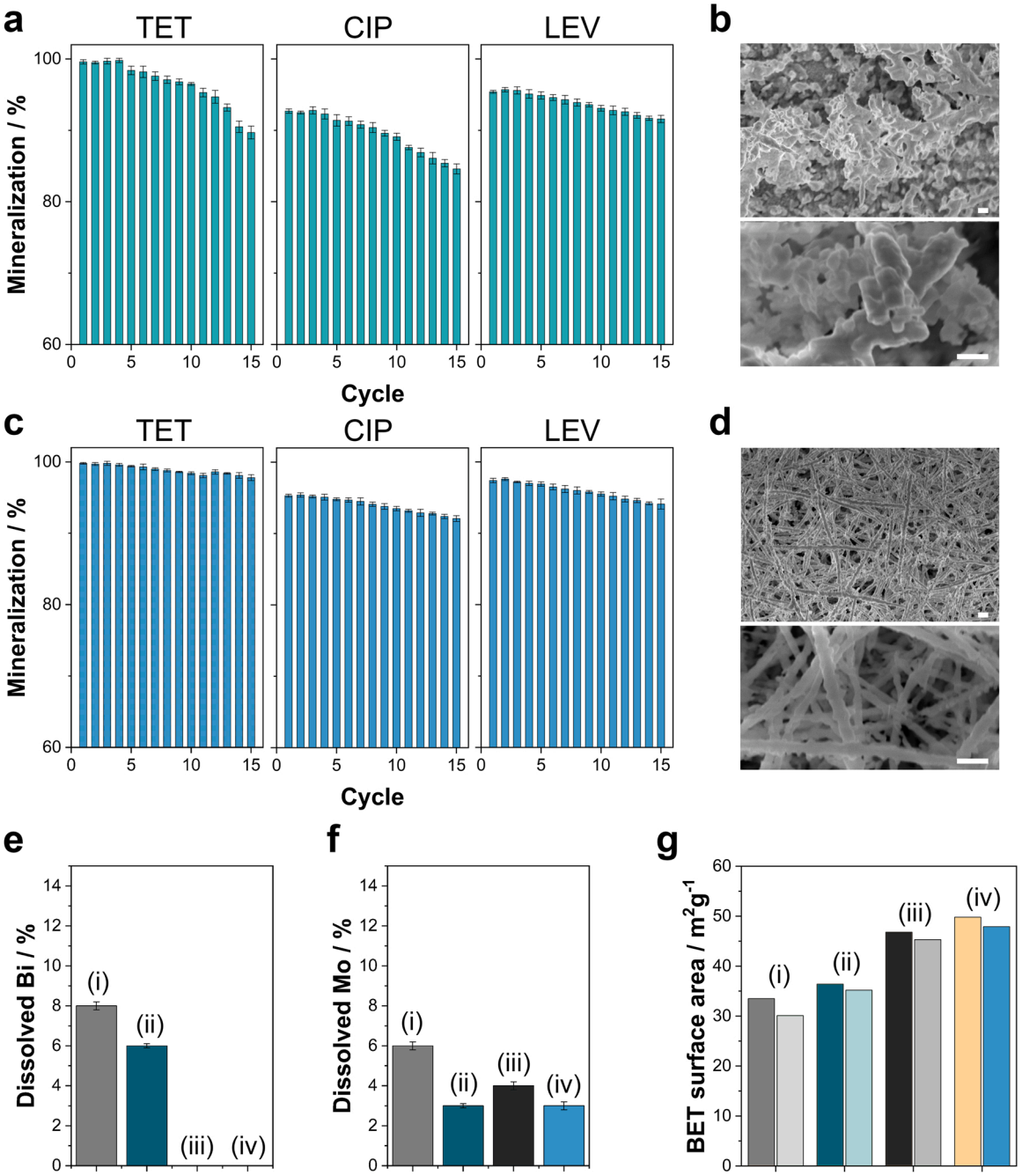

Fig. 8. : Reusability of the Bi_2MoO_6@Bi_2MoO_{6-x} homojunction photocatalysts prepared at (a) −0.9 V (i) and (c) −1.3 V (iii) in 15 consecutive cycles of 180 min. The figure also shows FE-SEM micrographs of the Bi_2MoO_6@Bi_2MoO_{6-x} homojunction photocatalysts prepared at (b) −0.9 V and (d) −1.3 V for 15 consecutive cycles (scale bar: 500 nm), the percentage of (e) dissolved bismuth and (f) dissolved molybdenum relative to their initial amounts in each photocatalyst, and (g) the variation of BET's surface area after 72 h of the continuous visible-light irradiation of the Bi_2MoO_6 and Bi_2MoO_6@Bi_2MoO_{6-x} photocatalysts.

photocorrosion. Considering the conditions explored, the antibiotic mineralization ranking was as follows: Bi_2MoO_6 (–0.9 V) < Bi_2MoO_6 (–1.3 V) < Bi_2MoO_6@Bi_2MoO_{6-x} (–0.9 V) < Bi_2MoO_6@Bi_2MoO_{6-x} (–1.3 V). That ranking shows that the oxygen vacancies play an important role in the process by promoting the adsorption of molecular oxygen, which, as an electron scavenger, interacts with photogenerated electrons to reduce the rate of the pernicious recombination of photogenerated holes with the electrons. The electrodeposition method combined with thermal treatment presented is thus a new method of preparing customized bismuth–molybdenum Aurivillius deposits with effective photocatalytic capabilities. The proven reuse and the low photocorrosion observed in the presence of the contaminant are other added values that recommend further work on the photocatalyst's implementation in real cases using solar radiation.

CRediT authorship contribution statement

Elvira Gómez: Conceptualization, Validation, Funding acquisition, Project administration, Resources, Writing – review & editing. **Roberto Cestaro**: Conceptualization, Methodology, Formal analysis, Data curation, Writing – original draft. **Laetitia Philippe**: Conceptualization, Funding acquisition, Project administration, Resources, Writing – original draft. **Albert Serrà**: Conceptualization, Methodology, Conceptualization, Investigation, Software, Data curation, Validation, Funding

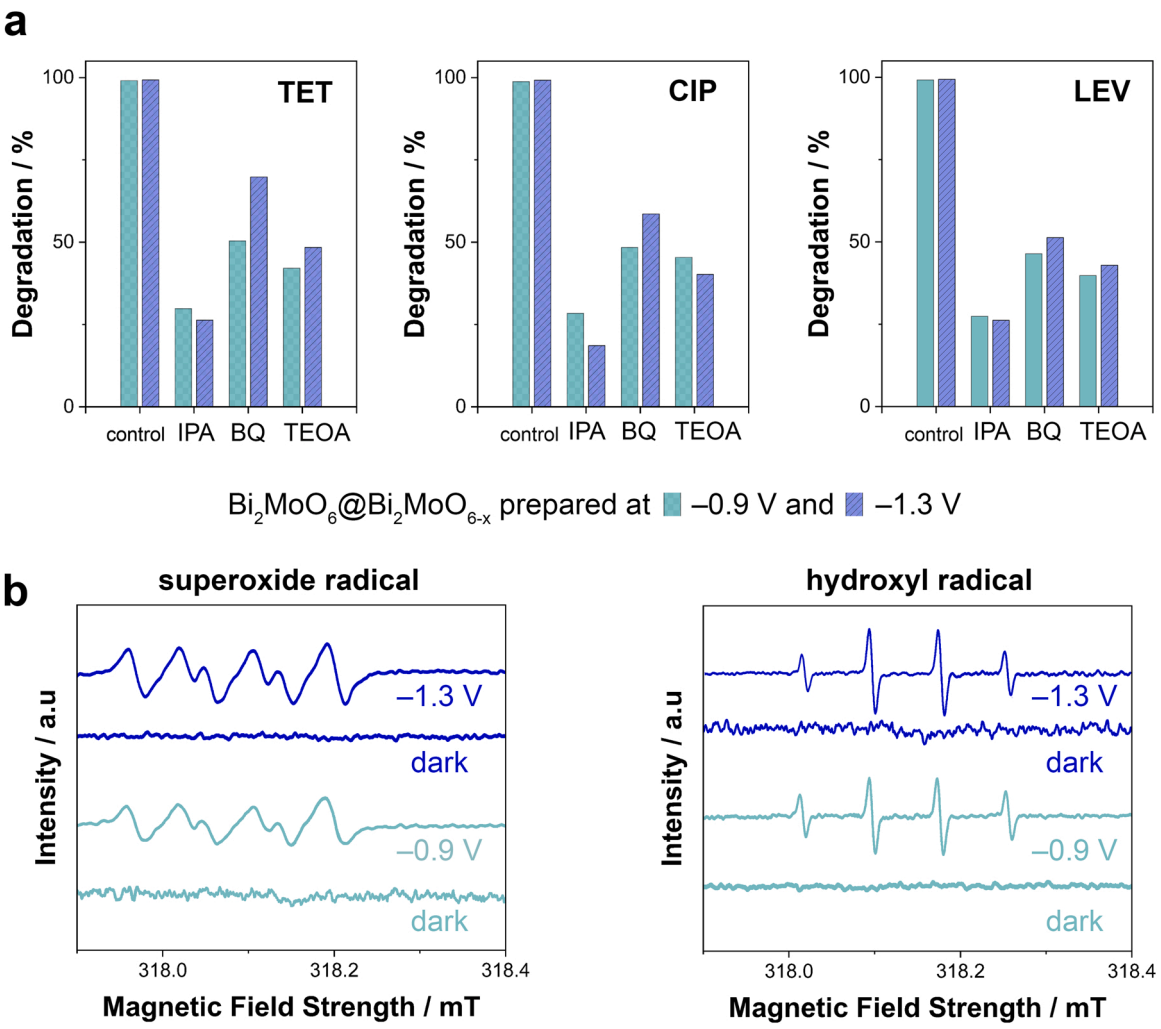

Fig. 9. : (a) Trapping of active species during the photocatalytic degradation of single-pollutant solutions of TET (20 ppm), CIP (20 ppm), and LEV (20 ppm) at 20 °C after 180 min of visible-light irradiation. (b) EPR spectra of the Bi_2MoO_6@Bi_2MoO_{6-x} homojunction photocatalysts prepared at −0.9 V and −1.3 V with DMPO obtained in dark and visible irradiation in methanol to detect DMPO-$^{\bullet}O_2^-$ and in water to detect DMPO-$^{\bullet}$OH.

acquisition, Project administration, Resources, Writing – original draft, Writing – review & editing. All authors discussed the results and commented on the manuscripts.

Declaration of Competing Interest

The authors declare that they have no known competing financial interests or personal relationships that could have appeared to influence the work reported in this paper.

Data Availability

No data was used for the research described in the article.

Acknowledgements

Grant PID2020-115663GB-C32 funded by *Ministerio de Ciencia e Innovación/Agencia Estatal de Investigación* (MCIN/ AEI/10.13039/ 501100011033). Authors thank the CCiT-UB for the use of their equipment.

Appendix A. Supporting information

Supplementary data associated with this article can be found in the online version at doi:10.1016/j.apcatb.2022.121703.

References

[1] A. Serrà, E. Gómez, J. Michler, L. Philippe, Facile cost-effective fabrication of Cu@Cu_2O@CuO–microalgae photocatalyst with enhanced visible light degradation of tetracycline, Chem. Eng. J. 413 (2021), https://doi.org/10.1016/j.cej.2020.127477.

[2] D. Wang, F. Jia, H. Wang, F. Chen, Y. Fang, W. Dong, G. Zeng, X. Li, Q. Yang, X. Yuan, Simultaneously efficient adsorption and photocatalytic degradation of tetracycline by Fe-based MOFs, J. Colloid Interface Sci. 519 (2018) 273–284, https://doi.org/10.1016/j.jcis.2018.02.067.

[3] A. Bembibre, M. Benamara, M. Hjiri, E. Gómez, H.R. Alamri, R. Dhahri, A. Serrà, Visible-light driven sonophotocatalytic removal of tetracycline using Ca-doped ZnO nanoparticles, Chem. Eng. J. 427 (2022), https://doi.org/10.1016/j.cej.2021.132006.

[4] M.E.A. de Kraker, A.J. Stewardson, S. Harbarth, Will 10 million people die a year due to antimicrobial resistance by 2050? PLoS Med. 13 (2016) 1–6, https://doi.org/10.1371/journal.pmed.1002184.

[5] C.J. Murray, K.S. Ikuta, F. Sharara, L. Swetschinski, G. Robles Aguilar, A. Gray, C. Han, C. Bisignano, P. Rao, E. Wool, S.C. Johnson, A.J. Browne, M.G. Chipeta, F. Fell, S. Hackett, G. Haines-Woodhouse, B.H. Kashef Hamadani, E.A.P. Kumaran, B. McManigal, R. Agarwal, S. Akech, S. Albertson, J. Amuasi, J. Andrews, A. Aravkin, E. Ashley, F. Bailey, S. Baker, B. Basnyat, A. Bekker, R. Bender, A. Bethou, J. Bielicki, S. Boonkasidecha, J. Bukosia, C. Carvalheiro, C. Castañeda-Orjuela, V. Chansamouth, S. Chaurasia, S. Chiurchiù, F. Chowdhury, A.J. Cook, B. Cooper, T.R. Cressey, E. Criollo-Mora, M. Cunningham, S. Darboe, N.P.J. Day, M. De Luca, K. Dokova, A. Dramowski, S.J. Dunachie, T. Eckmanns, D. Eibach, A. Emami, N. Feasey, N. Fisher-Pearson, K. Forrest, D. Garrett, P. Gastmeier, A. Z. Giref, R.C. Greer, V. Gupta, S. Haller, A. Haselbeck, S.I. Hay, M. Holm, S. Hopkins, K.C. Iregbu, J. Jacobs, D. Jarovsky, F. Javanmardi, M. Khorana,

N. Kissoon, E. Kobeissi, T. Kostyanev, F. Krapp, R. Krumkamp, A. Kumar, H.H. Kyu, C. Lim, D. Limmathurotsakul, M.J. Loftus, M. Lunn, J. Ma, N. Mturi, T. Munera-Huertas, P. Musicha, M.M. Mussi-Pinhata, T. Nakamura, R. Nanavati, S. Nangia, P. Newton, C. Ngoun, A. Novotney, D. Nwakanma, C.W. Obiero, A. Olivas-Martinez, P. Olliaro, E. Ooko, E. Ortiz-Brizuela, A.Y. Peleg, C. Perrone, N. Plakkal, A. Ponce-de-Leon, M. Raad, T. Ramdin, A. Riddell, T. Roberts, J.V. Robotham, A. Roca, K.E. Rudd, N. Russell, J. Schnall, J.A.G. Scott, M. Shivamallappa, J. Sifuentes-Osornio, N. Steenkeste, A.J. Stewardson, T. Stoeva, N. Tasak, A. Thaiprakong, G. Thwaites, C. Turner, P. Turner, H.R. van Doorn, S. Velaphi, A. Vongpradith, H. Vu, T. Walsh, S. Waner, T. Wangrangsimakul, T. Wozniak, P. Zheng, B. Sartorius, A.D. Lopez, A. Stergachis, C. Moore, C. Dolecek, M. Naghavi, Global burden of bacterial antimicrobial resistance in 2019: a systematic analysis, Lancet 399 (2022) 629–655, https://doi.org/10.1016/S0140-6736(21)02724-0.

[6] J. O'Neill, Tackling drug-resistant infections globally: final report and recommendations: the review on antimicrobial resistance; 2016 [Available from: ⟨https://amr-review⟩. org, Publ. Html. (2019) 1–35. ⟨https://amr-review.org/sites/default/files/160518_Final⟩ paper_with cover.pdf.

[7] P. Verlicchi, M. Al Aukidy, E. Zambello, Occurrence of pharmaceutical compounds in urban wastewater: Removal, mass load and environmental risk after a secondary treatment-A review, Sci. Total Environ. 429 (2012) 123–155, https://doi.org/10.1016/j.scitotenv.2012.04.028.

[8] J.A.I. Pimentel, C. Di Dong, S. Garcia-Segura, R.R.M. Abarca, C.W. Chen, M.D.G. de Luna, Degradation of tetracycline antibiotics by Fe^{2+}-catalyzed percarbonate oxidation, Sci. Total Environ. 781 (2021), https://doi.org/10.1016/j.scitotenv.2021.146411.

[9] A. Serrà, L. Philippe, F. Perreault, S. Garcia-Segura, Photocatalytic treatment of natural waters. Reality or hype? The case of cyanotoxins remediation, Water Res 188 (2021), https://doi.org/10.1016/j.watres.2020.116543.

[10] M.N. Chong, B. Jin, C.W.K. Chow, C. Saint, Recent developments in photocatalytic water treatment technology: A review, Water Res 44 (2010) 2997–3027, https://doi.org/10.1016/j.watres.2010.02.039.

[11] C.V. Manzano, L. Philippe, A. Serrà, Recent progress in the electrochemical deposition of ZnO nanowires: synthesis approaches and applications, Crit. Rev. Solid State Mater. Sci. (2021) 1–34, https://doi.org/10.1080/10408436.2021.1989663.

[12] M.R. Hoffmann, S.T. Martin, W. Choi, D.W. Bahnemann, Environmental Applications of Semiconductor Photocatalysis, Chem. Rev. 95 (1995) 69–96, https://doi.org/10.1021/cr00033a004.

[13] E. Brillas, A. Serrà, S. Garcia-Segura, Biomimicry designs for photoelectrochemical systems: Strategies to improve light delivery efficiency, Curr. Opin. Electrochem. 26 (2021), https://doi.org/10.1016/j.coelec.2020.100660.

[14] H.O.N. Tugaoen, S. Garcia-Segura, K. Hristovski, P. Westerhoff, Challenges in photocatalytic reduction of nitrate as a water treatment technology, Sci. Total Environ. 599–600 (2017) 1524–1551, https://doi.org/10.1016/j.scitotenv.2017.04.238.

[15] R. Yang, Z. Zhu, C. Hu, S. Zhong, L. Zhang, B. Liu, W. Wang, One-step preparation (3D/2D/2D) $BiVO_4/FeVO_4$@rGO heterojunction composite photocatalyst for the removal of tetracycline and hexavalent chromium ions in water, Chem. Eng. J. 390 (2020), 124522, https://doi.org/10.1016/j.cej.2020.124522.

[16] H. Yu, L. Jiang, H. Wang, B. Huang, X. Yuan, J. Huang, J. Zhang, G. Zeng, Modulation of Bi_2MoO_6-based materials for photocatalytic water splitting and environmental application: a critical review, Small 15 (2019) 1–30, https://doi.org/10.1002/smll.201901008.

[17] Z. Ni, Y. Sun, Y. Zhang, F. Dong, Fabrication, modification and application of $(BiO)_2CO_3$ -based photocatalysts: a review, Appl. Surf. Sci. 365 (2016) 314–335, https://doi.org/10.1016/j.apsusc.2015.12.231.

[18] Z. Dai, F. Qin, H. Zhao, J. Ding, Y. Liu, R. Chen, Crystal defect engineering of aurivillius Bi_2MoO_6 by Ce doping for increased reactive species production in photocatalysis, ACS Catal. 6 (2016) 3180–3192, https://doi.org/10.1021/acscatal.6b00490.

[19] G. Tian, Y. Chen, W. Zhou, K. Pan, Y. Dong, C. Tian, H. Fu, Facile solvothermal synthesis of hierarchical flower-like Bi_2MoO_6 hollow spheres as high performance visible-light driven photocatalysts, J. Mater. Chem. 21 (2011) 887–892, https://doi.org/10.1039/c0jm03040f.

[20] L. Zhang, T. Xu, X. Zhao, Y. Zhu, Controllable synthesis of Bi_2MoO_6 and effect of morphology and variation in local structure on photocatalytic activities, Appl. Catal. B Environ. 98 (2010) 138–146, https://doi.org/10.1016/j.apcatb.2010.05.022.

[21] H. Shen, F. Fu, W. Xue, X. Yang, S. Ajmal, Y. Zhen, L. Guo, D. Wang, R. Chi, In situ fabrication of Bi_2MoO_6/Bi_2MoO_{6-x} homojunction photocatalyst for simultaneous photocatalytic phenol degradation and Cr(VI) reduction, J. Colloid Interface Sci. 599 (2021) 741–751, https://doi.org/10.1016/j.jcis.2021.04.122.

[22] J. Guo, L. Shi, J. Zhao, Y. Wang, K. Tang, W. Zhang, C. Xie, X. Yuan, Enhanced visible-light photocatalytic activity of Bi_2MoO_6 nanoplates with heterogeneous Bi_2MoO_{6-x}@Bi_2MoO_6 core-shell structure, Appl. Catal. B Environ. 224 (2018) 692–704, https://doi.org/10.1016/j.apcatb.2017.11.030.

[23] M. Wang, M. You, K. Zhang, Y. Zhang, J. Han, R. Fu, S. Liu, T. Zhu, $Bi_{3.64}Mo_{0.36}O_{6.55}/Bi_2MoO_6$ heterostructure composite with enhanced photocatalytic activity for organic pollutants degradation, J. Alloy. Compd. 766 (2018) 1037–1045, https://doi.org/10.1016/j.jallcom.2018.07.062.

[24] L. Zhou, W. Wang, L. Zhang, Ultrasonic-assisted synthesis of visible-light-induced Bi_2MO_6 (M = W, Mo) photocatalysts, J. Mol. Catal. A Chem. 268 (2007) 195–200, https://doi.org/10.1016/j.molcata.2006.12.026.

[25] X. Li, S. Fang, L. Ge, C. Han, P. Qiu, W. Liu, Synthesis of flower-like Ag/AgCl-Bi_2MoO_6 plasmonic photocatalysts with enhanced visible-light photocatalytic performance, Appl. Catal. B Environ. 176–177 (2015) 62–69, https://doi.org/10.1016/j.apcatb.2015.03.042.

[26] H.H. Li, K.W. Li, H. Wang, Hydrothermal synthesis and photocatalytic properties of bismuth molybdate materials, Mater. Chem. Phys. 116 (2009) 134–142, https://doi.org/10.1016/j.matchemphys.2009.02.058.

[27] F.L. Zheng, G.R. Li, X.L. Yu, Y.X. Tong, Synthesis of bismuth molybdate nanowires via electrodeposition-heat- treatment method, Electrochem. Solid-State Lett. 12 (2009) 56–59, https://doi.org/10.1149/1.3143909.

[28] Z.-Q. Liu, L.-Y. Tang, N. Li, K. Xiao, J. Wang, J.-H. Zhang, Y.-Z. Su, Y.-X. Tong, Facile synthesis of large-area hierarchical bismuth molybdate nanowires for supercapacitor applications, J. Electrochem. Soc. 159 (2012) D582–D586, https://doi.org/10.1149/2.014210jes.

[29] M. Zargazi, M.H. Entezari, Bi_2MoO_6 nanofilms on the stainless steel mesh by PS-PED method: photocatalytic degradation of diclofenac sodium as a pharmaceutical pollutant, Ultrason. Sonochem. 62 (2020), 104867, https://doi.org/10.1016/j.ultsonch.2019.104867.

[30] M. Zargazi, M.H. Entezari, Ultrasound assisted deposition of highly stable self-assembled Bi_2MoO_6 nanoplates with selective crystal facet engineering as photoanode, Ultrason. Sonochem. 67 (2020), https://doi.org/10.1016/j.ultsonch.2020.105145.

[31] M.S. Sayed, D. Mohapatra, M.L. Baynosa, J.J. Shim, Three-dimensional core-shell heterostructure of tungsten trioxide/bismuth molybdate/cobalt phosphate for enhanced photoelectrochemical water splitting, J. Colloid Interface Sci. 598 (2021) 348–357, https://doi.org/10.1016/j.jcis.2021.03.105.

[32] A. Quintana, A. Varea, M. Guerrero, S. Suriñach, M.D. Baró, J. Sort, E. Pellicer, Structurally and mechanically tunable molybdenum oxide films and patterned submicrometer structures by electrodeposition, Electrochim. Acta 173 (2015) 705–714, https://doi.org/10.1016/j.electacta.2015.05.112.

[33] E. Gómez, E. Pellicer, E. Vallés, Intermediate molybdenum oxides involved in binary and ternary induced electrodeposition, J. Electroanal. Chem. 580 (2005) 238–244, https://doi.org/10.1016/j.jelechem.2005.03.031.

[34] D. Sinkeviciute, J. Baltrusaitis, N. Dukstiene, Layered molybdenum oxide thin films electrodeposited from sodium citrate electrolyte solution, J. Solid State Electrochem. 15 (2011) 711–723, https://doi.org/10.1007/s10008-010-1137-2.

[35] M. Gacitua, Y. Boutaleb, L. Cattin, S. Yapi Abe, Y. Lare, G. Soto, G. Louarn, M. Morsli, R. Rehamnia, M.A. Del Valle, A. Drici, J.C. Bernède, Electrochemical preparation of MoO_3 buffer layer deposited onto the anode in organic solar cells, Phys. Status Solidi Appl. Mater. Sci. 207 (2010) 1905–1911, https://doi.org/10.1002/pssa.200925602.

[36] E. Gómez, E. Pellicer, E. Vallés, Detection and characterization of molybdenum oxides formed during the initial stages of cobalt-molybdenum electrodeposition, J. Appl. Electrochem 33 (2003) 245–252, https://doi.org/10.1023/A:1024136909641.

[37] Y. Da Tsai, C.H. Lien, C.C. Hu, Effects of polyethylene glycol and gelatin on the crystal size, morphology, and Sn^{2+}-sensing ability of bismuth deposits, Electrochim. Acta 56 (2011) 7615–7621, https://doi.org/10.1016/j.electacta.2011.06.077.

[38] S. Jiang, Y.H. Huang, F. Luo, N. Du, C.H. Yan, Synthesis of bismuth with various morphologies by electrodeposition, Inorg. Chem. Commun. 6 (2003) 781–785, https://doi.org/10.1016/S1387-7003(03)00104-7.

[39] F. Fu, H. Shen, W. Xue, Y. Zhen, R.A. Soomro, X. Yang, D. Wang, B. Xu, R. Chi, Alkali-assisted synthesis of direct Z-scheme based Bi_2O_3/Bi_2MoO_6 photocatalyst for highly efficient photocatalytic degradation of phenol and hydrogen evolution reaction, J. Catal. 375 (2019) 399–409, https://doi.org/10.1016/j.jcat.2019.06.033.

[40] F. Fu, H. Shen, X. Sun, W. Xue, A. Shoneye, J. Ma, L. Luo, D. Wang, J. Wang, J. Tang, Synergistic effect of surface oxygen vacancies and interfacial charge transfer on Fe(III)/Bi_2MoO_6 for efficient photocatalysis, Appl. Catal. B Environ. 247 (2019) 150–162, https://doi.org/10.1016/j.apcatb.2019.01.056.

[41] X.Y. Kong, Y.Y. Choo, S.P. Chai, A.K. Soh, A.R. Mohamed, Oxygen vacancy induced Bi_2WO_6 for the realization of photocatalytic CO_2 reduction over the full solar spectrum: from the UV to the NIR region, Chem. Commun. 52 (2016) 14242–14245, https://doi.org/10.1039/c6cc07750a.

[42] N. Li, H. Gao, X. Wang, S. Zhao, D. Lv, G. Yang, X. Gao, H. Fan, Y. Gao, L. Ge, Novel indirect Z-scheme g-C_3N_4/Bi_2MoO_6/Bi hollow microsphere heterojunctions with SPR-promoted visible absorption and highly enhanced photocatalytic performance, Chin. J. Catal. 41 (2020) 426–434, https://doi.org/10.1016/S1872-2067(19)63478-9.

[43] R.F. Howe, M. Grätzel, EPR study of hydrated anatase under UV irradiation, J. Phys. Chem. 91 (1987) 3906–3909, https://doi.org/10.1021/j100298a035.

[44] Y. Nakaoka, Y. Nosaka, ESR Investigation into the effects of heat treatment and crystal structure on radicals produced over irradiated TiO_2 powder, J. Photochem. Photobiol. A Chem. 110 (1997) 299–305, https://doi.org/10.1016/S1010-6030(97)00208-6.

[45] V. Ischenko, S. Polarz, D. Grote, V. Stavarache, K. Fink, M. Driess, Zinc oxide nanoparticles with defects, Adv. Funct. Mater. 15 (2005) 1945–1954, https://doi.org/10.1002/adfm.200500087.

[46] D. Wang, H. Shen, L. Guo, C. Wang, F. Fu, Y. Liang, Ag/Bi_2MoO_{6-x} with enhanced visible-light-responsive photocatalytic activities via the synergistic effect of surface oxygen vacancies and surface plasmon, Appl. Surf. Sci. 436 (2018) 536–547, https://doi.org/10.1016/j.apsusc.2017.12.002.

[47] J. Hou, S. Cao, Y. Wu, F. Liang, Y. Sun, Z. Lin, L. Sun, Simultaneously efficient light absorption and charge transport of phosphate and oxygen-vacancy confined in bismuth tungstate atomic layers triggering robust solar CO_2 reduction, Nano Energy 32 (2017) 359–366, https://doi.org/10.1016/j.nanoen.2016.12.054.

[48] Y. Lv, W. Yao, R. Zong, Y. Zhu, Fabrication of wide-range-visible photocatalyst Bi_2WO_{6-x} nanoplates via surface oxygen vacancies, Sci. Rep. 6 (2016) 1–9, https://doi.org/10.1038/srep19347.
[49] Y. Zheng, T. Zhou, X. Zhao, W.K. Pang, H. Gao, S. Li, Z. Zhou, H. Liu, Z. Guo, Atomic interface engineering and electric-field effect in ultrathin Bi_2MoO_6 nanosheets for superior lithium ion storage, Adv. Mater. 29 (2017) 1–8, https://doi.org/10.1002/adma.201700396.
[50] Z. Ma, P. Li, L. Ye, Y. Zhou, F. Su, C. Ding, H. Xie, Y. Bai, P.K. Wong, Oxygen vacancies induced exciton dissociation of flexible BiOCl nanosheets for effective photocatalytic CO_2 conversion, J. Mater. Chem. A. 5 (2017) 24995–25004, https://doi.org/10.1039/c7ta08766g.
[51] H.T. Bui, S. Weon, J.W. Bae, E.J. Kim, B. Kim, Y.Y. Ahn, K. Kim, H. Lee, W. Kim, Oxygen vacancy engineering of cerium oxide for the selective photocatalytic oxidation of aromatic pollutants, J. Hazard. Mater. 404 (2021), 123976, https://doi.org/10.1016/j.jhazmat.2020.123976.
[52] P. Peng, Z. Chen, X. Li, Y. Wu, Y. Xia, A. Duan, D. Wang, Q. Yang, Biomass-derived carbon quantum dots modified Bi_2MoO_6/Bi_2S_3 heterojunction for efficient photocatalytic removal of organic pollutants and Cr (Vl), Sep. Purif. Technol. 291 (2022), 120901, https://doi.org/10.1016/j.seppur.2022.120901.
[53] S. Dong, X. Liu, G. Tian, Y. Wang, G. Jin, Y. Zhao, J. Sun, M. Fan, Surface oxygen vacancies modified Bi2MoO6 double-layer spheres: enhanced visible LED light photocatalytic activity for ciprofloxacin degradation, J. Alloy. Compd. 892 (2022), 162217, https://doi.org/10.1016/j.jallcom.2021.162217.
[54] S. Li, C. Wang, M. Cai, F. Yang, Y. Liu, J. Chen, P. Zhang, X. Li, X. Chen, Facile fabrication of $TaON/Bi_2MoO_6$ core–shell S-scheme heterojunction nanofibers for boosting visible-light catalytic levofloxacin degradation and Cr(VI) reduction, Chem. Eng. J. 428 (2022), 131158, https://doi.org/10.1016/j.cej.2021.131158.
[55] Z. Yin, S. Qi, S. Deng, K. Xu, Z. Liu, M. Zhang, Z. Sun, Bi_2MoO_6/TiO_2 heterojunction modified with Ag quantum dots: a novel photocatalyst for the efficient degradation of tetracycline hydrochloride, J. Alloy. Compd. 888 (2021), 161582, https://doi.org/10.1016/j.jallcom.2021.161582.
[56] J. Guo, L. Wang, X. Wei, Z.A. Alothman, M.D. Albaqami, V. Malgras, Y. Yamauchi, Y. Kang, M. Wang, W. Guan, X. Xu, Direct Z-scheme $CuInS_2/Bi_2MoO_6$ heterostructure for enhanced photocatalytic degradation of tetracycline under visible light, J. Hazard. Mater. 415 (2021), 125591, https://doi.org/10.1016/j.jhazmat.2021.125591.
[57] W. Shi, M. Li, X. Huang, H. Ren, F. Guo, Y. Tang, C. Lu, Construction of $CuBi_2O_4/Bi_2MoO_6$ p-n heterojunction with nanosheets-on-microrods structure for improved photocatalytic activity towards broad-spectrum antibiotics degradation, Chem. Eng. J. 394 (2020), 125009, https://doi.org/10.1016/j.cej.2020.125009.
[58] S. Chen, D. Huang, G. Zeng, X. Gong, W. Xue, J. Li, Y. Yang, C. Zhou, Z. Li, X. Yan, T. Li, Q. Zhang, Modifying delafossite silver ferrite with polyaniline: visible-light-response Z-scheme heterojunction with charge transfer driven by internal electric field, Chem. Eng. J. 370 (2019) 1087–1100, https://doi.org/10.1016/j.cej.2019.03.282.
[59] F. Chen, G.X. Huang, F.B. Yao, Q. Yang, Y.M. Zheng, Q.B. Zhao, H.Q. Yu, Catalytic degradation of ciprofloxacin by a visible-light-assisted peroxymonosulfate activation system: performance and mechanism, Water Res. 173 (2020), 115559, https://doi.org/10.1016/j.watres.2020.115559.
[60] T. An, H. Yang, G. Li, W. Song, W.J. Cooper, X. Nie, Kinetics and mechanism of advanced oxidation processes (AOPs) in degradation of ciprofloxacin in water, Appl. Catal. B Environ. 94 (2010) 288–294, https://doi.org/10.1016/j.apcatb.2009.12.002.
[61] J. Deng, Y. Ge, C. Tan, H. Wang, Q. Li, S. Zhou, K. Zhang, Degradation of ciprofloxacin using A-MnO_2 activated peroxymonosulfate process: effect of water constituents, degradation intermediates and toxicity evaluation, Chem. Eng. J. 330 (2017) 1390–1400, https://doi.org/10.1016/j.cej.2017.07.137.
[62] S. Song, C. Lu, X. Wu, S. Jiang, C. Sun, Z. Le, Strong base g-C_3N_4 with perfect structure for photocatalytically eliminating formaldehyde under visible-light irradiation, Appl. Catal. B Environ. 227 (2018) 145–152, https://doi.org/10.1016/j.apcatb.2018.01.014.
[63] A.A. Isari, M. Mehregan, S. Mehregan, F. Hayati, R. Rezaei Kalantary, B. Kakavandi, Sono-photocatalytic degradation of tetracycline and pharmaceutical wastewater using WO_3/CNT heterojunction nanocomposite under US and visible light irradiations: a novel hybrid system, J. Hazard. Mater. 390 (2020), 122050, https://doi.org/10.1016/j.jhazmat.2020.122050.
[64] X. Ma, H. Li, T. Liu, S. Du, Q. Qiang, Y. Wang, S. Yin, T. Sato, Comparison of photocatalytic reaction-induced selective corrosion with photocorrosion: Impact on morphology and stability of Ag-ZnO, Appl. Catal. B Environ. 201 (2017) 348–358, https://doi.org/10.1016/j.apcatb.2016.08.029.
[65] M. Benamara, E. Gómez, R. Dhahri, A. Serrà, Enhanced photocatalytic removal of cyanotoxins by Al-Doped ZnO nanoparticles with visible-LED irradiation, Toxins 13 (2021), https://doi.org/10.3390/toxins13010066.